Author/s:
Salerno, VM;Capitanio, FA;Farrington, RJ;Riel, N

Title:
The role of long-term rifting history on modes of continental lithosphere extension

Date:
2016-11-10

Citation:
Salerno, V. M., Capitanio, F. A., Farrington, R. J. & Riel, N. (2016). The role of long-term rifting history on modes of continental lithosphere extension. JOURNAL OF GEOPHYSICAL RESEARCH-SOLID EARTH, 121 (12), pp.8917-8940. https://doi.org/10.1002/2016JB013005.

Persistent Link:
https://hdl.handle.net/11343/292124

The role of long-term rifting history on modes of continental lithosphere extension

V. Morena Salerno *, Fabio A. Capitanio, Rebecca J. Farrington[1] and Nicolas Riel[2]
School of Earth, Atmosphere and Environment, Monash University, Clayton, 3800 VIC, Australia
School of Earth Sciences, University of Melbourne, Australia
Department of Earth Sciences, Durham University, UK

Key words
Rifting history; Lithosphere extension; Basin subsidence, melting.

Highlights
- Numerical models link rifting histories to lithospheric extension modes and basin types
- We provide tools to decipher the style of basin types, subsidence patterns and melt production.
- We highlight cases in which rifting history cannot be neglected.

ABSTRACT

Continental lithosphere extension results in complex basin types with differing structural styles, subsidence, thermal histories and melt production. Many studies have examined the role of initial rheological layering, geothermal gradients and extension rates during a single rifting event. This approach neglects the tectonic history of many basins that are marked by multiple rifting events. Here, we address the role of repeated extension on long-term lithospheric strain modes and the resulting basins, highlighting cases most affected by previous rifting events. We use numerical models of a lithosphere undergoing two rifting events of differing extension rates and separated by cooling, to show the effect of early events on subsequent evolution. The combination of boundary displacement velocity in both events leads to the formation of various rift basin types, ranging from narrow to wide to hyper-extended, and with variation of subsidence patterns, degrees of symmetry and melt yield. We show that basin type, subsidence and melt production might be strongly affected by previous rifting events, illustrating cases in which the previous rifting history cannot be neglected. Our models reproduce the first-order features of Earth's sedimentary basins, and propose a classification to guide the interpretation of extensional basins and their evolution.

1. INTRODUCTION

The major effect of tectonic divergence on continental lithosphere is rifting, with

lithosphere undergoing stretching and thinning. Rifting results in faulting, subsidence, sedimentary basin formation, and can lead to episodic magmatism (e.g. *Mckenzie*, 1978; *Wernicke and Burchfiel*, 1982; *Wernicke*, 1985; *Kusznir and Park*, 1987; *Buck*, 1991; *Brun*, 1999). Many different rift basin types are observed on Earth, ranging from wide to narrow (i.e., basins wider/narrower than the average lithospheric thickness), to those with hyper-thinned crust, and asymmetric structures (e.g. *Brune et al.*, 2012, 2013, 2014, 2016; *Brun*, 1999; *Buck*, 1991; *Huismans and Beaumont*, 2007,2011, 2014; *Keen*, 1985, 1987a, 1987b; *Kusznir and Park*, 1987; *Perez-Gussinye et al.*, 2006; *Perez-Gussinye*, 2012; *Peron-Pinvidic and Manatschalm*, 2010; *Peron-Pinvidic et al.*, 2015; *Lavier & Manatschal*, 2006). The variety of rift basins and passive margins is evidence that the same physical process can develop in contrasting ways over time and space. Yet, we do not have a clear understanding of how and why these divergences take place. In particular, a more general approach to explain the emergence of rift basin diversity during lithospheric extension is still lacking.

Basin types are often associated with two end-member lithospheric-scale strain modes: 1) the localized strain mode, where lithosphere extension and thinning affect a confined region, with a width smaller than lithospheric thickness, and 2) the distributed strain mode, where strain affects a region with a width greater then lithosphere thickness (*England*, 1983, *Kuszmir and Park* 1987; *Buck*, 1991, *Bassi*, 1991; *Crameri and Kaus*, 2010). Hence, in this paper we refer to distributed and localized strain meaning weakly and strongly localized strain, respectively. The first mode considers coupled crust and lithospheric mantle strain throughout the whole lithosphere, observed in narrow basins such as Northern Red Sea, East African Rift and the Rhine graben (e.g. *Buck*, 1991; *Gueydan et al.*, 2008; *McKenzie*, 1978). Conversely, the second mode considers uncoupled crust and lithospheric mantle strain (e.g. *Buck*, 1991; *Wernicke*, 1985), often associated with hot lithosphere, and observed in wide basins such as the Basin and Range province (*Buck*, 1991; *Brun*, 1999). This uncoupled tectonics style also applies to basins with strongly thinned crust overlying unroofed lithospheric mantle, as observed on hyper-extended margins such the Iberian margin (e.g. *Whitmarsh* et al., 2001; *Hopper et al.*, 2004; *Unternehr et al.*, 2010; *Aslanian and Moulin*, 2010; *Huismans and Beaumon*t, 2011; *Manatschal et al.*, 2015). The record of these basins may include episodic melting during rifting, identified by deep high velocity bodies, as observed along the northern Iberian continental margin (*Zelt et al.*, 2003) and northern Angolan margin (*Moulin et al.*, 2005) or volcanism, as observed in the African Rift System (*Corti*, 2012 and references therein; *Schmeling*, 2010: *Baker et al.*, 1972) and several volcanic margins along the Atlantic Ocean (e.g. *Franke*, 2013).

Our knowledge on selection of lithosphere strain mode and sedimentary basin type formation, relies on models of rifting processes. Rifting is modelled, and therefore largely understood, as a single event of lithospheric extension. During this event the surface subsides forming a sedimentary basin, followed by a post-rifting cooling period, when lithospheric thermal thickening controls subsidence (*McKenzie*, 1978).

The single rifting event modeling approach helps to highlighted the role of the lithospheres initial and tectonic boundary conditions during rifting. These models show that the selection of lithospheric strain modes and consequent basin types, emerge from the competition between the initial rheological stratification, geothermal gradients (e.g. *Buck*, 1991; *Gueydan et al*., 2008*; Weinberg et al*., 2007), boundary extension rates and tensile force variations (e.g. *van Wijk and Cloetingh*, 2002; *England*, 1983). *Buck* (1991) proposed that a distributed strain mode results from extension of a hot lithosphere with an elevated initial surface heat flow, Q_s = 80 mW/m^2, thus defined as weak lithosphere. The model with thickened crust (40 km) was used to explain the evolution of the North Basin and Range, and Aegean Sea wide basins (*Buck*, 1991). Conversely, a localized strain mode results from extension of a cold lithosphere with a lower initial surface heat flow, Q_s = 60 mW/m^2, thus defined as strong lithosphere. A model with a normal crust thickness (30 km) is used to explain the formation of narrow basins such as Rio Grande, Northern Red Sea, Gulf of Suez, East African Rifts, Rhine Graben and Baikal Rift (*Buck*, 1991). *Gueydan et al*., (2008) show that increasing (decreasing) the mantle-crust thickness ratio increases (decreases) the coupling between crust and lithospheric mantle, therefore favoring a lithospheric strain localized (distributed) strain mode. *Gueydan et al*., (2008) use this approach to explain the evolution of Basin and Range, and Corinth wide basins; the formation of Limagne-Bress-Rhine, Rio Grande, East African Rift, and Baikal rifting systems narrow basins; and the deep crustal décollement along the Atlantic-type non-volcanic passive margins. *Van Wijk and Cloetingh* (2002) show that rifting velocities, imposed through boundary displacement, exert a similar control on lithosphere strain mode selection, expressed by strain localization width, with wide/narrow basins forming under conditions of constant slow/fast extension. *Van Wijk and Cloetingh* (2002) use their modelling results to explain the evolution of the mid-Norwegian, Galicia and South Alpine margins.

To date a generalized explanation on how the rifting process can produce these many rift basin types, with a wide range of different characteristics, is missing. An attempt to embed the controlling parameters into a unified understanding has been proposed in *Kaus and Podladchikov* (2006) and *Crameri and Kaus* (2010). In these

works, the known conditions necessary for lithosphere strain localization are accounted for in a localization index, highlighting the controls of plastic thickness, temperature-dependent viscosity, Moho temperature and initial strain-rates on rifting evolution. *Lu et al.* (2011) applied this approach to the rifting evolution on the North China Craton province, confirming the strong controls of lithospheric strain modes on the emergence of different rift basin types.

However, these published models assume the effect of a single rifting event and specific initial conditions, making generalization difficult. Many geological cases include complex strain histories characterized by multiple rifting events, alternating with quiescence, variation of subsidence patterns, time-dependent displacement velocities, rifting migration and melting episodes. One such case is the Norway margin (*Gabrielsen et al.*, 1999; *Reemst and Cloetingh*, 2000), where the rifting history includes several rifting events (290-235 Ma, 170-95 Ma, 75-57 Ma) ending in oceanization by ~ 55 Ma. Similar rifting histories are observed in the Iberian Basin (*van Wees et al*., 1998), West Antarctic Rift System (*Huerta and Harry*, 2007; *Corti et al*., 2013), Michigan Basin (*Bond and Kominz*, 1984), Lybia's Sirte Basin (*Capitanio et al*., 2009), South China Sea (*Chen*, 2014) and many others (see *Şengör and Natal'in*, 2001).

Interpreting complex extensional settings as the result of a single rifting event remains problematic (e.g. *Allen and Armitage*, 2012). Only a few authors have attempted an alternative approach to the problem, describing complex settings observed in specific areas, through the interaction of several rifting events and quiescence periods. During rifting events thermo-mechanical perturbations arise, while during the period of quiescence, cooling of the thermal lithosphere occurs. *Van Wees et al*. (1998) illustrated the role of multiple rifting events separated by tectonic quiescence and thermal subsidence in the Iberian Basin. *Chen* (2014), used a rifting-cooling-rifting cycle to model the subsidence in the Baiyun Sag along the continental slope of the South China Sea. A similar modeling strategy was adopted by *Ali and Watts* (2013) and *Cunha* (2008) to interpret the subsidence history of the Gulf of Aden and the Iberia margin, respectively. *Armitage et al*. (2010) invoked multiple rifting events alternating with cooling periods to explain strain migrations and magma production in the Greenland and South-West Indian margins. *Huismans and Beaumont* (2007) also showed how cooling between rifting events favors deeper strain localization in the mantle, resulting in an asymmetric basin and exhumation of mantle lithosphere, compatible with that observed in the Newfoundland–Iberia margin system. The role of cooling between rifting events on basin migration and margin asymmetry has also been investigated by *Naliboff and Buiter* (2015), focusing on the mid-Norwegian and mid-East Greenland margins, and the Northern and

Southern Atlantic passive margins. *Petersen et al*. (2015), also studied the role of the cooling period on subsidence patterns in long-term rifting.

A general understanding of the role of rifting history on lithosphere strain modes, still needs to be proposed. In particular, a generalized and simplified understanding of the effect repeated rifting events has on basin evolution, not driven by the application to specific geological examples, is still missing. Here, we aim to constrain the role of rifting history on the final basin type and extract a general classification of the conditions under which previous strain events affect rifting evolution. We follow a forward modeling approach with the purpose to gain general insights on the rifting process using models rather than from a specific geological example. Numerical models are used to reproduce different rifting histories by extension of a lithosphere. This is achieved using identical rheological layering and initial conditions with differing boundary conditions. A range of extension rates are applied during two isolated rifting events, separated by a cooling period when extension vanishes. The result is a range of diverse basin types, including wide and narrow basins, different degrees of symmetry, basins on hyper-thinned crust and sag-like basins. We quantify the thinning factor of the crust and lithospheric mantle, tectonic subsidence and melting histories, providing comparative tools to geological observables. In particular, we identify patterns of rifting evolution that are strongly controlled by previous rifting events and those that are independent of early rift history. We conclude by discussing insights into the interpretation of key features of lithosphere extension modes and basins types, and their relevance for understanding the rifting process and basins reconstructions.

2. NUMERICAL MODELING

2.1. Modeling approach

Our modeling approach focuses on the lithosphere extending under horizontal stretching, resulting in thinning of the crust and lithospheric mantle, and surface depression, producing a rift basin. Results are presented using common tools of basin analysis including, crust and mantle thinning factors, β and δ, (i.e. *Huismans et al.,* 2001; *England, 1983*; *van Wijk and Cloetingh,* 2002), melt production rates and volumes (i.e. *van Wijk et al*., 2001). See Appendix B for full details on the calculation of thinning factors, melt production rate and volumes.

The strain of the lithosphere under extension is modelled by imposing boundary velocities, and by focusing on the role of the variation of boundary conditions during rifting, i.e. the velocity of boundary displacement. We perform modeling in 2D, using

an identical initial layered lithospheric model for each simulation, including the same equilibrium continental geotherm and rheological parameters (Table 1).

Rifting history is modelled in three stages: an initial rifting event, a cooling period and a second rifting event. Each rifting event stops at the same finite horizontal strain, $\varepsilon = L_0/L$, where L_0 is the initial model width and L the final. For a model of initial width 400 km, the first rifting event stops at a width of 464 km, ($\Delta\varepsilon$ = 1.16), the second event stops when the width reaches 528 km ($\Delta\varepsilon$ =1.32.). The duration of each rifting event, t_r, depends on the velocity of boundary displacement, v, calculated using $t_r = L_0 \Delta\varepsilon / v$.

We consider the lithosphere as the thermal boundary layer (TBL), comprising the crust and lithospheric mantle. Under extension, the crust thins mechanically and localizes, while the lithospheric mantle thins thermally, creating a thermal perturbation at the base of the lithosphere. This perturbation can be characterized using its width and the vertical upward deflection of the Lithosphere-Asthenosphere Boundary (LAB): when the velocity of boundary displacement is large, the thermal perturbation is narrow and high; when the velocity of boundary displacement is small, the thermal perturbation is wide and short. During the cooling period thermal diffusion restores the steady state geotherm, allowing the lithosphere to regain most of the original thickness. Thus, cooling time duration can be parameterized as a function of thermal thinning of the lithospheric mantle at the end of first rifting event. Defining the thickness, a, of a thermal boundary layer (the lithosphere) through the depth of the isotherm 1300 ˚C yields $a = c\,(\kappa t)^{1/2}$ (*Turcotte and Schubert*, 2014), with κ thermal diffusivity, t time and c a constant. Thus, the cooling time, t_c, needed to restore the isotherm to initial position depends on its displacement, and can be quantified using the lithospheric mantle thinning factor δ (see Appendix B):

$$t_c = \frac{h^2}{c^2\kappa}\left(1 - \frac{1}{\delta}\right)^2 \quad (1)$$

where the non-dimensional constant c = 0.85 is determined empirically.

Cooling by diffusion allows the growth of the thermal boundary layer, counteracting lithospheric thinning. This process can be quantified using the non-dimensional Péclet number (Pe), which measures the ratio between isotherm advection and thermal diffusion during thinning (*England*, 1983; *Allen and Armitage*, 2012; *Allen and Allen*, 2013). The Péclet number can be calculated as $Pe = \dot{\varepsilon} a^2/2\kappa$, where $\dot{\varepsilon} = du/dl$ is the strain rate (*Allen and Allen*, 2013; *Allen and Armitage*, 2012). This illustrates that the transition from diffusion- to advection-

dominated processes is dependent on strain rate. The two end-members, dominated by either diffusion or advection, correlate to one of the two transition pathways, from distributed to localized strain mode (wide and narrow rifting modes), discussed in *Buck* (1991), providing a relationship between slow/fast extension rates with cool/warm lithospheres. The other way indicates that at the same strain rate the transition can be controlled by crustal buoyancy (*Buck*, 1991). Therefore, although we have modelled a wide range of velocities, in the remainder of the paper we refer to two velocities of boundary displacement, v_{slow} and v_{fast}, indicating two values that clearly lead to one of these two deformation modes. A result of this process is that diffusion and advection balance during extension under very slow velocities, resulting in no evident thermal perturbations. This implies that in a range of models, the cooling period vanishes and the two rifting events are replaced by a long-term deformation until the finite strain is achieved.

In our models, the Péclet number during the first rifting event are Pe < 2 for diffusion dominated models and Pe > 8 for advection dominated. These values are found to be in good agreement with *Allen and Allen* (2013) and *England* (1983), showing that model results are independent of the chosen modelling approach (e.g. initial parameters, model setup).

The use of two sets of boundary displacement velocities (v_{slow} set and of v_{fast} set), provides four groups of models: two groups with the same velocity in both rifting events and two groups where the velocities are different for the two rifting event. Thus, we use a nomenclature for the models based on the applied velocity of boundary displacement, with r for the slow rifting of v_{slow} and R for the fast rifting of v_{fast}. Hence, we define four end-member models: 1) r_1-r_2, 2) r_1-R_2, 3) R_1-r_2 and 4) R_1-R_2, where the subscript 1 and 2 indicate the first and the second rifting events respectively. We have used a total of 17 velocities in both rifting events, for a total of 17 x 17 = 289 models.

In our approach we do not focus on isostasy or tectonic structures within rift basins, such as faulting, sedimentary infill. While these would affect the depth and the inner architecture of the basins (the basin type), they do not impact lithospheric rifting mode (*Bialas and Buck*, 2009). However, in order to reconcile our results with the available body of work on extensional basins, these are accounted for when calculating tectonic subsidence, i.e. net sediment load under the assumption of isostasy.

2.2 Model set up

We use the Underworld geodynamics code for the models (*Moresi et al.*, 2007;

Moresi et al., 2003). Details of the governing equations and rheological laws used can be found in the Appendix A.

The governing equations (Appendix A, Eq.1A, Eq.2A, and Eq.3) are solved in a 2D computational domain 700 km deep and 400 km wide, with a spatial grid resolution of 1 km x 1 km (Fig. 1) and 20 Lagrangian particles per element. The upper and lower crust is composed of two 15 km thick layers. The lithospheric mantle, extending beneath the crust to the bottom of the domain has homogeneous material properties differentiated into lithospheric and asthenospheric mantle by a temperature-dependent viscosity (Appendix A, Eq. 8A) For simplicity, hereafter we will refer to the lithospheric mantle as mantle and take the crust and lithospheric mantle together to be the lithosphere. The mechanical stiffness of the lithosphere is, thus, loosely constrained, and we define the Lithosphere-Asthenosphere Boundary (LAB) as the 1300 °C isotherm (*Schmeling*, 2010), located initially at a depth of 100 km. Atop the upper crust we use an air layer 40 km thick, this "sticky air" allows for a quasi-free surface and self-consistent evolution of topography (*Crameri et al.*, 2012).

We consider layers with no pre-existing perturbation in the lithosphere, i.e. no weak/strong seeds or thermal anomalies are introduced (*Fernandez and Ranalli*, 1997). Despite being commonly used in numerical modeling as a prerequisite for strain localization (*Peters et al.*, 2015, and references therein), these heterogeneities can constrain the nucleation process of strain localization, predetermining where the instability nucleates and presides (*Peters et al.*, 2015). This favors lithospheric necking and localized strain, thus restricting the range of lithospheric strain modes. While we have performed rigorous resolution tests to select the most efficient finest grid, we are aware that strain localization within numerically homogenous materials may be affected by numerical approximations, introducing heterogeneities (*Peters et al.*, 2015). While this is outside the scope of this paper, the inferences on strain localization and strain distribution remains valid, as localization simply occurs at a larger strain/strain rate, with the same features (e.g. *Schmeling*, 2010). The absence of initial perturbations in the model setup was adopted by *Crameri and Kaus* (2010), who considered lithospheric localization to be regulate by the thickness of the plastic field.

The thicknesses of the lithosphere layers are tracked by Lagrangian passive tracers embedded in the models' surface (top of the upper crust), the top and base (Moho) of the lower crust and the initial LAB.

The initial temperature distribution in the model follows that of an equilibrated continental geotherm (*Allen and Allen*, 2013) with temperature boundary conditions

of T_0 = 0 °C at the surface and T_{lab} = 1300 °C at the base of the lithosphere, and a Moho temperature of 600 ˚C. The temperature field in the crust T_c and mantle T_m are defined as:

$$T_c = T_0 + \left(\frac{Q_m + H_r h}{k}\right)a - \frac{H_r}{2k}h^2 \quad (2)$$

$$T_m = T_c + \left(\frac{Q_m}{k}\right)(a - h) \quad (3)$$

where Q_m is the heat flux from the mantle, H_r is the radiogenic heat production, h is the thickness of the whole crust, k is the thermal conductivity, a is the thickness of the lithosphere $a = h + H$, and H the lithosphere mantle thickness. Deeper, the temperature is kept constant. On the top and bottom of the model space we enforce free-slip boundary conditions, whereas on the side we apply kinematic boundary conditions. The side walls of the model domain are pulled with a constant velocity of v on the right side and $-v$ on the left side. These are consistent with the range of present-day plate velocities derived from GPS data and extrapolated over time (e.g. *Argus and Hefin*, 1995; *Reilinger and McClusky*, 2011; *McClusky et al*., 2010). To provide a more general understanding, we will express the velocity boundary conditions as initial strain-rates, $\dot{\varepsilon} = v/L_0$, for each rifting event. The velocity range, $2v$, of 0.1 to 6 cm/yr (Table 1) and domain's initial width of 400 km, produce initial strain-rates of 7.9×10^{-17} s^{-1} to 4.7×10^{-15} s^{-1}, comparable to those recovered from geological cases (*Newman and White*, 1999). The strain-rate inside the lithosphere varies as $\dot{\varepsilon}(t) = \dot{\varepsilon}\, exp(-t\dot{\varepsilon})$ (*England*, 1983), which implies strain-rates remain significant for times $\dot{\varepsilon}^{-1}$. We use $\dot{\varepsilon}_i$, with i = 1, 2, to indicate the initial strain-rate due to the constant velocity imposed at the i-th rifting event.

We have performed additional tests changing the horizontal size of the domain, resolution, initial crust thickness, rheological parameters, radiogenic heating and adding weak/strong seeds in order to investigate their effect. We note that only models with an initial perturbation, such as weak/strong seeds, result in earlier strain localization, strongly constraining the evolution, while none of the other parameters produced a significant deviation. For clarity we present a reduced set of models.

3. RESULTS

In this section we analyze the thinning factors, subsidence curves and melt production of the 289 modelled rifting histories. We identify 4 main rifting history patterns, describing them using end-member models. We first describe the slow first

rifting event models, r_1-r_2 and r_1-R_2 (Sections 3.1 and 3.2), followed by those with a fast first rift event, R_1-r_2 and R_1-R_2 (Sections 3.3 and 3.4). The cooling periods are identified as c_q for models r_1-r_2 and r_1-R_2, and C_q for R_1-r_2 and R_1-R_2. This helps to categorize the 289 models into 4 basin type groups, highlighting relationships and transition regimes (Section 3.5.1). We calculate and analyze the lithosphere localization indexes for the 289 models and compare them with basin type groups (Section 3.5.2).

Note that in this paper we use the terms coupled and decoupled to indicate when the rheological layers have the same strain mode. That is the crust and mantle are coupled if they both deformed in either a distributed or localized strain mode. The rheological layers are considered decoupled if they deform under differing strain modes.

3.1 Model r_1-r_2

3.1.1 Strain modes and thinning

Event r_1

The evolution of the crustal and mantle thinning factors, β and δ, shows the development of different strain modes in the crust and mantle (Appendix B, Eq. 1B and 2B). Fig. 2 shows the time evolution of β and δ factors by rift event and cooling period.

The r_1 event runs for 22 Myr with v_{slow} = 0.15 cm/yr, stopping when horizontal strain $\Delta\varepsilon$ reaches 64 km (Fig. 2a, b and Fig. 3a, d). The crust and mantle are uniformly thinned throughout the domain with time. The crust reaches an average β ~1.2 at the end of r_1 (Fig. 2a). At the domain center, two locations develop larger crustal thinning with the maximum β = 1.35: here, the crust thickness reduces from the initial 30 km to 22 km. The mantle thins less compared to the crust, with $\delta \leq 1.08$ (Fig. 2a): mantle thickness reduces from the initial 70 km to ~ 65 km. The β and δ factors both increase progressively over the domain, showing the lithosphere deforming in a distributed strain mode during the r_1 event (Fig. 2a, Fig. 3a).

Fig. 3 represents the second invariant of the strain rate, $\dot{\varepsilon}_{II}$, at the end of the first rifting events, r_1 and R_1 (Fig. 3a and d), and at the end of the second rifting events, r_2 (Fig.3 b and c) and R_2 (Fig.3 e and f). The LAB at the end of the first rifting event (Fig. 3a, d red line) and at the end of cooling periods (Fig. 3a, d black horizontal line) are also shown.

In Fig. 3a event r_1 is characterized by a low *Pe* number, *Pe* < 2, with heat diffusion dominating advection. It correlates the diffuse strain mode to the low velocity boundary displacement (*England*, 1981; *van Wijk and Cloetingh*, 2002). Thus allowing the LAB to displace almost uniformly upward across the domain, with a slight doming thermal perturbation located in the model center (Fig. 3a, red line). At the end of r_1, several distributed thin shear zones are present, with max $\dot{\varepsilon}_{II}$ < $1.2x10^{-15}$ s^{-1}: the whole lithosphere deforms following a distributed strain mode (Fig. 3a), associated with a wide rifting mode (e.g. *Buck*, 1991; *England*, 1981, *van Wijk and Cloetingh*, 2002; *Lu et al.*, 2011).

Cooling c_q

The crust thinning factor β remains constant during the cooling period, c_q, with the Moho depth remaining unchanged (Fig, 2a, b right panel) and a crust 22 km thick. However, the mantle thinning factor δ decreases (Fig. 2a,b left panels) from a thickness of 65 km with $\delta \leq 1.08$ at the end of r_1, to 77 km with $\delta = 0.91$ at the end of c. The lithospheric mantle recovers the total thickness lost during the previous rifting event, with a total TBL thickness of 99 km at the end of c_q.

Thermal diffusion is the only heat transfer mechanism active during lithospheric cooling, allowing isotherms to relax and equilibrate. This allows the LAB to restore to its original position (Fig. 3a, from red to black line). At the end of the cooling period, the lithospheres rheological structure has a thickened, cold mantle and a thinned crust. Both vertical and horizontal strength distributions are affected by the variability of crust/mantle thickness ratio along the lithosphere (*Naliboff and Buiter*, 2015).

Event r_2

Fig. 2b shows β and δ thinning factors for the second-rifting event r_2, with the same velocity boundary displacement v_{slow} = 0.15 cm/yr as for r_1. The onset of crust localized thinning occurs rapidly upon extension in r_2 and is marked by the emergence of two distinct depressions. These two locations record larger crust thinning, where β exceeds 3.5. Note, these are the two points where the crustal thinning factor was slightly higher at the end of the r_1 event. These inherited rheological heterogeneities play a major role in final basin geometry. In this case, the heterogeneities result in an asymmetric surface rift basin of ~280 km width, with the main depression located above the thinned mantle, and the secondary depression located over the non-thinned mantle. Mantle thinning remains almost negligible at the beginning of r_2, with an average $\delta = 0.93$. At 34 Myr this slowly increases to $\delta = 0.98$

until 37 Myr. At ~38 Myr the mantle localizes in a small area, with a maximum δ = 1.6 at the end of r_2, corresponding with the largest crustal thinning location.

β and δ show that during the majority of the r_2 event, strain modes in the crust and mantle remain distributed and coupled. Only toward the end of r_2 does the mantle change from distributed to localized strain mode, leading to decoupling between crust and mantle.

Fig. 3b shows the second invariant of the strain rate, $\dot{\varepsilon}_{II}$, at the end of r_2. At this time the lithosphere strain is accommodated by two shear zones joined at the surface, with $\dot{\varepsilon}_{II} < 9x10^{-15}$ s^{-1}. The Péclet number for this event is $Pe < 2$, with diffusion the dominant heat transport mechanism (*England*, 1981; *van Wijk and Cloetingh*, 2002), as seen by the small thermal perturbation ~200 km wide and a vertical LAB displacement of ~15 km. Fig 3b shows that at the end of model r_1-r_2, the decoupled strain in the crust and mantle results in a wide basin, with asymmetry developing from inherited heterogeneities and growing at differing times under slow extension.

We conclude that the lithosphere history represented by model r_1-r_2, leads to the formation of an Asymmetric Wide Basin type (AWB).

3.1.2 Subsidence

In Fig. 4, we show the subsidence curves for multiple events (r_1-r_2 blue, r_1-R_2 orange, R_1-r_2 red and R_1-R_2 green). Breakup is shown to help characterize the full rifting history. Subsidence curves for three single rifting event models are shown for comparison (Fig. 4 M_0, M1 and M_2, black curves). For calculation see Appendix B (Eq. 3B).

Fig. 4 (blue, segment 1-2) shows a subsidence rate for event r_1 of 34 m Myr^{-1}: r_1 reaches a max subsidence of ~ 800 m in 22 Myr. This low subsidence rate reflects the relationship between slow lithospheric horizontal stretching ($\Delta\varepsilon$) and thinning (β, δ) and, therefore, the balance between heat diffusion and advection during lithosphere extension. No breakup occurs at the end of r_1. Fig 4 (blue, segment 2-3) shows the cooling period of 6 Myr during which the subsidence rate reduces to 0.12 m Myr^{-1}, producing a thermally-controlled subsidence curve.

Rifting resumes at the beginning of r_2, Fig. 4 (blue, segment 3-4), with a subsidence rate similar to the previous rifting event r_1. An increased subsidence at ~ 42 Myr, producing a basin of depth ~2100 m. The subsidence curve deflects upwards as a consequence of thermal diffusion, reaching a maximum subsidence value at 58 Myr. No lithospheric breakup occurs.

3.1.3 Melt

Fig. 5 shows for each model: the melt production rate (Fig. 5a), the integrated melt volume (Fig. 5b), and the melt fraction (Fig. 5c) at the end of the rifting events. Model r_1-r_2 is represented by the blue lines in Fig. 5a (dashed) and Fig. 5b (solid), and in panels 1 and 2 of Fig. 5c. For calculation see Appendix B (Eq. 4B to 7B).

Slow extension results in stationary isotherms with no melt produced during the slow initial rifting event r_1 (Fig. 5a, Fig. 5b, Fig. 5c panel 1). Melt is produced from 56 Myr in the r_2 event, reaching a maximum of 8 km^3/Myr (Fig. 5a, blue dashed) and an integrated melt volume of 70 km^3 (Fig. 5b, blue solid). This corresponds to a melt fraction of 0.4%, located beneath the major shear zones (~75 km), affecting an area ~10 km wide (Fig. 5c, 1 and 2). Note the time of 56 Myr for melt production occurs after the required stretching of $\varepsilon = 1.32$ is achieved, yet has been included for reference.

3.2 Model r_1-R_2

Model r_1-r_2 and r_1-R_2 share the first rift event r_1 and cooling period c_q, therefore we analyze only the strain, subsidence and melt during R_2.

3.2.1 Strain modes and thinning

Event R_2

R_2 is a short-lived rifting event of 3 Myr, with v_{fast} = 2.5 cm/yr. The simulation is stopped once horizontal stretching, $\Delta\varepsilon$ = 64 km (Fig. 2b and Fig. 3c).

The onset of crustal deformation occurs immediately: the strain is distributed across the crust with an average β = 1.2, with only one major thinned location ~ 200 km wide, where $\beta > 4$ (Fig. 2b, right panel). This is because the two points where the crustal thinning factor was slightly higher at the end of r_1 are simultaneously amplified during R_2. This significantly changes the role of inherited rheological heterogeneities in surface geometry selection: the resulting basin is symmetric and ~ 200 km wide, with a single main depression located above the thinned mantle.

Mantle thinning develops soon after the onset of the second fast rifting event and propagates laterally from the domain center to a maximum width of ~ 80 km by the end of R_2, with a max δ = 3. Mantle deforms with a localized strain mode (Fig. 2b, right panel).

Fig. 2b shows crust and mantle have decoupled during R_2: the crust develops a distributed strain during R_2 while the mantle evolves with a localized strain.

At the end of R_2 (32 Myr), the strain remains localized along two shear zones joining at the surface, with $\dot{\varepsilon}_{II} > 9x10^{-15}$ s^{-1}. (Fig. 3c). The Péclet number for this event is $Pe > 8$: in R_2 advection dominates diffusion (*England*, 1981; *van Wijk and Cloetingh*, 2002). Consequently, the final thermal perturbation in R_2 is ~ 300 km wide and characterized by a 42 km upward deflection of the LAB, more pronounced in comparison to that of r_2.

At 32 Myr, model r_1-R_2 is characterized by the co-existence of a symmetrically distributed strain in the crust and localized strain in the mantle, resulting in a Symmetric Wide Basin type (SWB).

3.2.2 Subsidence

Rifting resumes in R_2, with a subsidence rate of 166 m/Myr (Fig. 4 orange curve, segment 3-5). At the end of R_2 the maximum subsidence of ~ 1150 m is rapidly achieved in less than 3 Myr, ending in breakup by 31 Myr (Fig. 4, black star).

3.2.3 Melt

Fast extension during R_2 leads to the rapid upward displacement of isotherms with consequent melt production (Fig. 5a, Fig. 5b, Fig. 5c panel 4). Event R_2 starts melt production soon after rifting onset (~30 Myr) with a rate of 102 km^3/Myr (Fig. 5a, orange dashed line). By 31 Myr, lithospheric breakup occurs (Fig. 5a, black star) with a maximum melt rate of ~ 110 km^3/Myr. The total volume produced by breakup is ~500 km^3 with a total of ~1050 km^3 produced by the end of R_2 (Fig. 5b, orange solid line). The maximum melting fraction is ~ 1.7 %, between ~ 40 and 100 km depth affecting an area ~50 km wide (Fig. 5c, panel 4),

3.3 Model R_1-r_2

3.3.1 Strain modes and thinning

Event R_1

Fig. 2c shows β and δ thinning factors for the first rifting event R_1, with velocity of boundary displacement v_{fast} = 2.5 cm/yr. The R_1 event lasts 3.5 Myr (Fig. 2c and d). The strain concentrates in a narrow area, with large thinning occurring in both the mantle and crust (Fig. 2c). The β factor reaches a maximum value of 2: the crust thins from 3 to 15 km. The maximum δ factor is 1.55 and the mantle thickness reduces from 70 to 45 km. Consequently, larger thinning is recovered during the 21 Myr long cooling period. The lithosphere deforming in a localized strain mode during

the R_1 event with high β and δ factors concentrate in a ~ 40 km wide area, negligible thinning is measured outside this location (Fig. 2c , Fig. 3d).

Fig. 3d shows strain strongly localized along two major conjugate shear zones cross-cutting the entire lithosphere, with $\dot{\varepsilon}_{II}$ of 5.3x10-15 s^{-1}. Event R_1 is characterized by a high Péclet number, $Pe > 8$, with advection dominating thermal diffusion: this links the localized strain mode to the high velocity boundary displacement (*England*, 1981; *van Wijk and Cloetingh*, 2002). The LAB (Fig. 3d, red line) is deflected upwards by ~20 km beneath the major shear zones. The resulting thermal perturbation is ~ 200 km wide. At the end of R_1, the lithosphere shows a localized strain mode and the formation of a narrow basin of ~100 km width (Fig. 2d). We associate the lithosphere localized strain mode observed at the end of R_2 with a narrow rifting mode (e.g. *Buck*, 1991; *England*, 1981, *van Wijk and Cloetingh*, 2002; *Lu et al*., 2011).

Cooling C_q

During the cooling period C_q, the crust thinning factor βremains constant (Fig. 2c,d right panels) with a 15 km thick crust. At the end of R_1 the mantle is 45 km thick with $\delta \leq 1.5$, during cooling this increase to 83 km with $\delta = 0.84$ (Fig. 2c,d left panels), giving a total TBL thickness of 98 km. Due to the larger thinning factors in R_1 the cooling period lasts 22 Myr.

Heat diffusion allows the LAB to restore to its original position (Fig. 3d, red to black line). The lithosphere rheological structure has a thickened, cold mantle and a thinned crust in a narrow column ~ 90 km in average width, while the lateral part preserves the original crust and mantle thickness. This strongly variable lateral crust/mantle thickness ratio affects both lithosphere vertical and horizontal strength distributions (*Naliboff and Buiter*, 2015).

Event r_2

The upper part of Fig. 2c shows β and δ thinning factors for the event r_2, where v_{slow} = 0.15 cm/yr. Thinning of the crust and mantle are co-located, however very different (Fig. 2d). Under the slow extension of r_2 the crust thins rapidly, reaching large β factors of up to 20 in ~ 10 Myr. The crust is severely thinned to a thickness of 0.75 km with a surface basin ~ 80 km wide. Thinning in the mantle starts later, at ~ 30 Myr and remains consistently low, reaching maximum values of $\delta = 1.7$, thinning to 50 km. This configuration has a hyper-thinned crustal basin on an unroofed cold mantle. This model shows that while the crust and mantle deform under the same

localized strain mode, onset can be at a different time (~26 Myr in the crust and ~ 34 Myr in the mantle) with only crustal breakup achieved.

Fig. 3d, shows that the lithosphere deformation developed at the end of model R_1-r_2 is characterized by two conjugate shear zones joining at the center of the basin, yet with a higher strain rate of $\dot{\varepsilon}_{II}$ ~7x10^{-15} $s^{-1?}$ The Péclet number for r_2 is $Pe > 8$: the effect of advection dominating thermal diffusion (*England*, 1981; *van Wijk and Cloetingh*, 2002) is the emergence of a limited thermal perturbation ~220 km wide and a vertical LAB displacement of ~20 km.

The final configuration of event r_2 is characterized by localized lithospheric strain with a hyper-thinned crust, locate in a basin ~200 km wide and an unroofed mantle. The model R_1-r_2 leads to crustal break-up (*Franke*, 2013). We refer to this basin type as a Hyper-Thinned Basin (HTB).

3.3.2 Subsidence

During the R_1 rifting event the subsidence rate is ~366 m/Myr reaching maximum subsidence of 1100 m in ~ 3 Myr. The following 22 Myr cooling period leads to a thermal subsidence rate of 27 m/Myr, reaching a total depth of ~ 1700 m at 25 Myr.

The subsidence rate during the r_2 rift is similar to the thermal subsidence period until 30 Myr. It then increases dramatically to 190 m/Myr, reaching ~ 2650 m in less than 5 Myr (Fig. 4, red curve). At 35 Myr the crust breaks up (Fig. 4, grey star) while the mantle continues thinning (Fig. 2c, Fig. 3e).

3.3.3 Melt

During event R_1, fast extension results in the isotherms upward deflection and consequent melt production (Fig. 5a, Fig. 5b, Fig. 5c panel 5 and 7). Melt reaches a maximum of 27 km^3/Myr (Fig. 5a, red dashed) and an integrated melt volume of 200 km^3 (Fig. 5b, red solid). Strain localization and the rise of isotherms leads to ~1.2% maximum melt production in 3 Myr (Fig. 5c, panels 5 and 7). Melt is produced at a depth ~ 45 to 95 km within ~ 30 km width. This area is aligned with maximum mantle thinning. During cooling, melt rate production rapidly decreases to zero (Fig. 6a) leaving melt/depleted mantle embedded in the new forming lithosphere. No melt is produced during the second rift event r_2 (Fig. 5a, Fig, 5b and Fig. 5c panel 6).

3.4 Model R_1-R_2

Model R_1-r_2 and R_1-R_2 share the first rift event R_1 and cooling period C_q, therefore we analyze only the strain, subsidence and melt during R_2.

3.4.1 Strain modes and thinning

The second rift event R_2 has v_{fast}= 2.5 cm/yr and reaches $\Delta\varepsilon$ = 64 km in 3 Myr (Fig. 2d and Fig. 3f). In both the crust and mantle, extreme thinning starts at the onset of the R_2 rifting event with localized strain developing in 3 Myr, leading to lithospheric break up (Fig. 2d). The maximum values of β and δ factor are > 20, with a 0.75 km thick crust and 4.25 km thick mantle. The strain effects ~ 125 km wide crustal area and ~ 100 km wide mantle area, with negligible strain in lateral regions. Model R_1-R_2 shows a strong strain coupling between crust and mantle and a localized strain mode (Fig. 2d).

At the end of R_2 (27 Myr), the lithospheric strain is accommodated along two narrow shear zones joining at the surface, with 4.30×10^{-14} s^{-1} (Fig. 3f). The Péclet number for this event is *Pe* > 8 with a strong advection effect (*England*, 1981; *van Wijk and Cloetingh*, 2002). The resulting final thermal perturbation is ~ 240 km wide, with an ~ 65 km LAB upward deflection.

At 27 Myr, model R_1-R_2 is characterized by a lithospheric localized strain mode, resulting in a surface Narrow Rift Basin (NB) (Fig. 3f).

3.4.2 Subsidence Analysis

Event R_2 reaches a maximum subsidence of ~ 2000 m in 3 Myr with the R_1-R_2 model reaching full breakup at 27 Myr (Fig 5, black star).

3.4.3 Melting histories

Model R_1-R_2 restarts melt production at 25 Myr (Fig. 5a and Fig. 5b, green dashed line). The melt rate production reaches 150 km^3/Myr and an integrated melt volume of 2000 km^3, by lithosphere break up (27 Myr). Melt production continues until 29 Myr, when it reaches an integrated melt volume of 4500 km^3 (Fig. 5a,b). At the end of R_2 the melt fraction increases dramatically, reaching values of ~ 3.9 % at depths between ~ 40 and 100 km and affecting a region ~ 100 km wide (Fig. 5c, panel 8).

Summarizing, more pronounced lithospheric localization develops in the second rifting event in all the end-member models, as all are strongly affected by the initial/inherited conditions. Yet, the basins and lithospheric thinning differentiate into

four types, as function of rifting history, generated by varying boundary velocity between rifting events.

3.5 Rifting histories, basin types and lithospheric deformation.

In this section we analyze the entire suite of 289 models, assessing the sensitivity of the final rift basin type on the variation of boundary displacement velocity (boundary conditions) and, therefore, rifting history (Fig. 6a). We compare these with the localization indexes calculated for the lithosphere relative to each rifting history (Fig.6b). See Appendix B for the definition and calculation of localization indexes (Eq. 8B).

We plot the results in a domain diagram of the initial strain-rates of rift event 1, $\dot{\varepsilon}_1$, against event 2, $\dot{\varepsilon}_2$ (Fig. 6a, b). The initial strain rate, $\dot{\varepsilon}_i$, is defined as the ratio between velocity of boundary displacement and model width at the onset of the rifting event.

3.5.1 Basin type categories and transitions

Fig. 6a shows the classification of rifting histories in two groups: 1) "slow-early rifting-controls", with strain at the end of the first rifting event is distributed (i.e. Fig. 2a,b; Fig.3a), and 2) "fast-early rifting-controls" with models that localize strain at the end of the first rifting event (Fig. 2c,d; Fig.3d). In Fig. 6a and b the threshold between the groups is indicated on the horizontal axis with I_1. On the basis of the initial strain-rates $\dot{\varepsilon}_2$, and recalling the basin classification in Sections 3.1, 3.2, 3.3 and 3.4, we define four domains: AWB, SWB, HTB and NB, with the end-member models, r_1-r_2, r_2-R_2, R_1-r_2 and R_1-R_2 represented by larger dots. Fig. 6a also shows the transition area between basin type domains (light grey), where we have observed mixed features. The analysis of these are outside the scope of this paper.

Slow rifting histories are characterized by $\dot{\varepsilon}_1$ and $\dot{\varepsilon}_2$ between $7.9\text{x}10^{-17}$ and $2.8\text{x}10^{-17}$ s^{-1}. In these models, a small and distributed thinning in the crust is achieved (β< ~1.06) (e.g. Fig. 3a) with no thinning occurring within the mantle as the isotherms restore during extension. The thermal re-equilibration leads to overall mantle thickening, so that crust thinning is simultaneously replaced by mantle material. Consequently, in these models there is no effective cooling period between the two rifting events: they effectively undergo single rifting event. For these low strain rates, model evolution is insensitive of velocities changes. Similar evolutions are observed in intra-cratoninc and sag basins (e.g. Chad Basin, Eyre Basin as Modern examples; Palaeozoic Michigan and Illinois basins or Permian–Mesozoic West Siberian Basin; *Allen et al.*, 2015). Although the comparison to models here

remains purely speculative, we refer to this domain as Sag Basin-like (Fig. 6a, SB domain).

Models develop into Asymmetric Wide Basins (AWB) when the initial strain-rate of the first event is between $\dot{\varepsilon}_1$=7.90x10^{-17} s^{-1} and 6.35x10^{-16} s^{-1}, followed by initial strain-rates $\dot{\varepsilon}_2$= 7.90x10^{-17} s^{-1} to 2.38x10^{-15} s^{-1} in the second event. For increasing $\dot{\varepsilon}_1$ and decreasing $\dot{\varepsilon}_2$, the basin types transition from AWB to Symmetric Wide Basins (SWB). For example, if the rifting-cooling-rifting cycle starts with a very low strain-rate $\dot{\varepsilon}_1$ = 7.9x10^{-17} s^{-1}, the AWB model passes to SWB basin type at values of $\dot{\varepsilon}_2$= 2.38x10^{-15} s^{-1}. Alternatively, for $\dot{\varepsilon}_1$= 6.35x10^{-16} s^{-1} the transition occurs at values of $\dot{\varepsilon}_2$=1.19x10^{-15} s^{-1}, emphasizing the role of a slow-early rifting event.

The models develop a SWB under both low $\dot{\varepsilon}_1$ and high $\dot{\varepsilon}_2$. The transition to the Narrow Basin (NB) domain occurs at a smaller $\dot{\varepsilon}_1$, hence the basin type become less dependent on the previous rifting event. Yet, for the maximum – Earth-like – initial strain-rates used here, the dependence has weakened but not vanished. Additionally, the transition to a different domain, where mixed behavior is observed, reduces with increasing $\dot{\varepsilon}_2$. The NB domain is characterized by the largest initial strain-rate interval occurring for values $\dot{\varepsilon}_1$ > 5.55x10^{-16} s^{-1}. However, this field expands to lower values with increasing $\dot{\varepsilon}_2$. The mild negative slope of the transition between the SWB and NB indicates a weaker dependence on early rifting events as initial strain-rates in the following event increase.

Basins on Hyper-Thinned crust (HTB) are defined by $\dot{\varepsilon}_1$ > 1.58x10^{-15} s^{-}1. A transitional mode is observed for $\dot{\varepsilon}_1$ > 5.55 x10^{-15} s^{-1}, and $\dot{\varepsilon}_2$ > 7.90x10^{-17} s^{-1}, extending to smaller $\dot{\varepsilon}_1$ with increasing $\dot{\varepsilon}_2$. The transitional domain area is largest for small initial strain-rates, wider in the $\dot{\varepsilon}_1$ direction, and slightly narrower in the $\dot{\varepsilon}_2$ direction. This mixed domain width is maximum from $\dot{\varepsilon}_1$ = 5.55 x10^{-16} s^{-1} to ~ 15x10^{-16} s^{-1}. It reduces to $\dot{\varepsilon}_1$ = 0.7 x10^{-16} s^{-1} -13x10^{-16} s^{-1} when equivalent initial strain-rates are imposed in the second rift event.

Fig. 6a shows that the final basin type of “slow-early rifting-controls” models are sensitive to previous rifting histories, while the “fast-early rifting-controls” group is influenced by the boundary condition of the second rift event.

3.5.2 Rifting history controls on localization

The occurrence of lithospheric strain modes can be expressed by a localization criterion proposed by *Kaus and Podladchikov* (2006) and *Crameri and Kaus* (2010), incorporating diverse controlling parameters (see Appendix B).

For a single deformation event, localized (distributed) lithospheric strain occurs for localization index $I > 1$ ($I < 1$), where high (low) initial strain-rate or cold (hot) lithosphere, favor lithospheric strain localization (distribution) (*Crameri and Kaus*, 2010; *Lu et al.*, 2011).

To highlight the role of previous rifting history, we calculate localization indexes for all 289 models, at the onset of the second rifting event, indicated as I_2. Thus, the calculation embeds the inherited rheology from the previous rift event (Appendix B, Eq. 8A). The I_2 contours are plotted on a $\dot{\varepsilon}_1$ vs. $\dot{\varepsilon}_2$ domain diagram (Fig. 6b). The black solid line, I_2=1, indicates the threshold between strain localization and distribution regions for the second rift event.

Fig. 6b supports a direct comparison with predictions for lithospheric localization of single rifting events. This allow to point out the deviations of our models results from the predictions of single rifting modelling approach (*Kaus and Podladchikov*, 2006; *Crameri and Kaus*, 2010; *Lu et al.*, 2011). On Fig. 6b, the vertical dashed line, indicating $I_1 = 1$, is the projection of the models first rifting event onto the second events plot. The I_1 values are comparable to those in *Crameri and Kaus* (2010) and *Lu et al.*, (2011). Thus, "slow-early rifting-controls" basin types in Fig. 6b reflect $I_1 < 1$, which promotes a distributed lithospheric strain in the first rift event, while "fast-early rifting-controls" basin types correspond to $I_1 > 1$, favoring localized lithospheric strain for the first rift event.

The I_2 contours illustrate the largest deviation from predicted localization, occurring for initial strain-rates below the threshold value of $\dot{\varepsilon}_1 \sim 0.7\text{x}10^{-15}$ s^{-1}. In this case, the previous strain history strongly controls localization. The I_2 contour slope becomes gradually steeper for initial strain-rates $\dot{\varepsilon}_1 > 0.2\text{x}10^{-15}$ s^{-1}. I_2 contours flatten above the threshold value of $\dot{\varepsilon}_1 \sim 0.7\text{x}10^{-15}$ s^{-1}, indicating the lithosphere's ability to localize strain is mostly dependent on the previous event and is controlled by $\dot{\varepsilon}_2$. Values of I_2 increase moderately from SB, AWB and HTB basin type domains toward SWB and further towards NB.

The overlap between the lithospheric localization index and the basin types plot (Fig, 6b) shows how lithospheric history-dependent modes feedback into basin architecture. In particular, it shows that basin type domains with $I_2 < 1$ are SB, part of AWB, the majority of HTB and partially SWB. Part of the transitional zone also falls into the lithospheric strain distribution region. The remaining part of SWB, the upper part of the HTB domain, all the rest of transitional zone and NB are above the lithospheric localization limit for the second event.

In summary, models in the "slow first rifting-controls" group, with $I_1 < 1$, show lithospheric strain modes strongly dependent on the first rifting events boundary

condition, $\dot{\varepsilon}_1$. Instead, a different scenario is found for $I_1 > 1$, with the models from the "fast first rifting-controls" group are almost independent of the first event's history and boundary conditions.

4. DISCUSSION

4.1. Inferences on interpretations of rifted continental basin evolution style

Here we discuss inferences from our results on the general understanding and interpretation of basin histories. Providing conclusions on specific geological cases is outside the scope of this paper and would divert from the general findings.

Many of the existing studies (i.e. *England*, 1983; *Kusznir and Park*, 1987; *Buck*, 1991; *Brun*, 1999; *van Wijk and Cloetingh*, 2002; *Huismans and Beaumont* 2003, 2007; *Gueydan, et al*.,2008; *Lu et al.*, 2011; *Chenin and Beaumon*, 2013) follow the uniform rifting model of *McKenzie* (1978), which is limited to a single major rifting event. Here, we have shown that analyzing a single event, while providing fundamental insights (e.g. *Allen and Armitage*, 2013; *McKenzie*, 1978), does not lead to a unique rifting evolution. Models based on a single rifting event approach, reproduce fundamental features, such as wide or narrow basins, yet strongly depend on the choice of initial conditions, i.e. Moho temperature, initial lithospheric layering and rheologies. Thus, rift histories are differentiated on the basis of initial conditions. Yet, these are difficult to constrain on Earth, where initial conditions are never the same and depend on the tectonic history. We have shown that, although the models share the same initial conditions, and undergo the same rifting event, with equal horizontal stretching and boundary velocity, they are unlikely to produce similar features if a more complex strain history is considered. Thus, consideration of the entire history, leads to the identification of evolutionary patterns otherwise unobserved, providing a set of matching observables that correlate to the rifting events, and that can support interpretations of basin evolution.

Earlier studies show that the lithospheric extension mode (i.e. localized or distributed strain) for a single deformation event, depends on temperature, composition and initial strain-rate (e.g *England*, 1983; *Kusznir and Park*, 1987; *Buck*, 1991; *Brun*, 1999; *van Wijk and Cloetingh*, 2002; *Huismans and Beaumont* 2003, 2007; *Gueydan, et al*., 2008; *Lu et al.*, 2011; *Chenin and Beaumon*, 2013). Our results point out that the lithospheric extension mode of earlier rifting events exerts a primary influence on the resulting basin type. In most cases, we find that taking into account only the previous rifting event and cooling period is sufficient to justify the deviation from predicted trends (e.g. *Buck*, 1991; *England*, 1983; *Kusznir and Park*,

1987; *Brun*, 1999; *van Wijk and Cloetingh*, 2002; *Huismans and Beaumont* 2003, 2007; *Gueydan, et al*., 2008; *Lu et al*., 2011).

The symmetry of wide rift models depends strongly on the entire rifting history (i.e. Fig. 2a-b, and Fig. 3c-d models r_1-r_1 and r_1-R_2; Fig. 6, AWR and SWR domains). However, narrow basins and those on hyper-thinned crust are sensitive only to the boundary conditions of the most recent rifting event (e.g. velocity of boundary displacement or initial strain-rates). In this case, under initial high strain-rates, a narrow basin with severe lithospheric necking and breakup is produced (Fig. 2d and Fig. 3f, model R_1-R_2; Fig. 6, NB domain). Alternatively, protracted low initial strain rates allow severe crustal thinning, with possible crust breakup and mantle unroofing (Fig. 2c and Fig. 3e, model r_1-R_2; Fig. 6, HTB domain).

Huismans and Beaumont, (2007), *Tett and Sawyer* (1996) and *Naliboff and Buiter* (2015) performed previous studies on the role of cooling and repeated rifting events. While our study confirms their findings on the role of lithosphere stiffening during cooling, we also find that the boundary conditions used to drive lithospheric extension plays a first order role on (1) the switch over time (e.g. Fig. 2b), (2) the co-existence (e.g. Fig. 3c) of localized and distributed strain modes and (3) the amplification of inherited heterogeneities (Fig. 3a and 3c).

More importantly, our study distinguishes the cases when the entire rift history is required from cases when the main/last rifting event is sufficient to model basin evolution (Fig. 6). The main difference of our study to *Naliboff and Buiter* (2015) is the absence of migration of the previous basin's deformation center (*England*, 1983). Nevertheless, our models show shifting of crustal thinning centers and the creation of new basins with similar migration observed in slow single rifting event models with $\varepsilon > 1.32$ (i.e. Fig. 2a and Fig. 3b, model r_1-r_1; Fig. 6, AWR domain).

We have kept our approach as general as possible and provide additional guidance on the interpretation of the rifting process evolution. Therefore, it does not apply to any particular geological case since. We believe this would only weaken the general understanding achieved within this study. Nevertheless, it can be used to interpret the evolution of areas such as the mid-Norwegian margin, with a complex history of multiple rifting events and cooling periods. Additionally, the Sirte Basin in Libya shows superimposed diverse basin types including the coexistence of two lithospheric strain modes and an abrupt strain-rate variation linked to changing boundary forces (*Capitanio et al*., 2009).

4.2. Inferences on interpretations of tectonic subsidence patterns and melting production

Subsidence patterns are usually interpreted under the assumption of a single

(main) rifting event (*McKenzie*, 1978). Although successful, many geological cases have shown anomalous subsidence with irregular patterns, structural complexities and magmatic evolutions which cannot be explained by single rifting event simulations. Previous studies have invoked a range of processes to explain these anomalous changes in subsidence, including: magmatic intrusions during the initial extensional phase (*Buck*, 2004), phase changes linked to increasing overburden (*Artyushkov*, 2007: *Kaus et al*., 2005; *Petrini et al*., 2001), protracted negative dynamic topography effects (e.g. *Flament et al*., 2013; *Heine et al*., 2008), far-field stress variations (e.g. *Birt et al*., 1997; *Lyngsie et al*., 2007; *Marotta et al*., 2000) and rapid decrease of rift strength (e.g. *Brune et al*., 2016).

Here we have shown that subsidence patterns are strongly affected by the strain history of the rifting process: the occurrence of previous rifting events always lead to subsidence systematically different to that predicted by single rifting events. This may explain the divergence from the anomalous subsidence predicted in single rift event models, thus limiting the contributions of other processes. (*Buck*, 2004; *Artyushkov*, 2007: *Kaus et al*., 2005; *Petrini et al*., 2001; *Flament et al*., 2013; *Heine et al*., 2008; *Birt et al*., 1997; *Lyngsie et al*., 2007; *Marotta et al*., 2000). Slow rifting events occurring on a previously necked lithosphere lead to different inferred subsidence rates. Initial slow rifting of a pristine lithosphere produces subsidence of ~800 m in ~20 Myrs (Fig.4,). While equivalent subsidence can be achieved in a second slow rifting event, the subsidence rates are different, with ~800 m of tectonic subsidence achieved in 30 Myrs. Equivalent subsidence can be achieved in < 8 Myrs when the second slow rifting follows a slow or fast rifting event, respectively (Fig.4). This is even more dramatic when rifting is achieved under fast extension. In this case, the calculated tectonic subsidence of ~1800 m during the fast rifting of pristine lithosphere, dramatically reduces to <500 m when the same rifting event occurs on previously rifted lithosphere, independent of the previous boundary velocity. Albeit general, these results are in agreement with *Ali and Watts* (2013), *Cunha* (2009) and *Chen* (2014) who used multiple event subsidence models to show the effect of rifting history in specific geological cases such as the Gulf of Aden (*Ali and Watts*, 2013), Iberian margin (*Cunha*, 2009) and Baiyun Sag in South China Sea (*Chen*, 2014).

We have found that rifting histories impact melt production. *Van Wijk et al*. (2001) modeled the mid-Norwegian margin lithosphere, proposing melt production occurred mostly in the late syn-rift phase, with modeled melt volumes consistent with observations. They concluded that mantle plumes (e.g. *White and McKenzie*, 1989) or small-scale convection (e.g. *Buck*, 1986; *Anderson*, 1994; *Keen and Boutilier*, 1995) are not always necessary to explain volcanic margin evolution. Instead dynamic processes related to lithospheric extension may enhance melt production sufficiently to explain the enigmatic melt volumes observed along volcanic rifts, such as the

African Rift System (*Corti et al.*, 2012, and reference therein; *Baker et al.*, 1972) and several other volcanic margins along the Atlantic Ocean (e.g. *Franke*, 2013). Our work confirms that long-term rifting may result in a very different melt production rate. In particular, the same single fast rifting event may lead to melt volumes much larger, up to ~10 and ~ 30 times (Fig.6), when this follows a previous slow and fast rift event, respectively. Melt fractions are similar to that found by *Brune et al.* (2014), with melt volumes corresponding to those estimated by *van Wijk et al.* (2001). Most importantly, our study confirms *Armitage et al.* (2010) results on the role of rifting histories in explaining anomalous melt volumes calculated for the Greenland and South-west Indian margins.

5. CONCLUSION

We performed a 2D numerical modeling study testing the role of different rifting histories on lithospheric strain mode. We found rifting histories have a strong feedback on basin type, subsidence pattern and magma production.

In our models, rifting histories are controlled by the variation of boundary conditions during two rifting events separated by tectonic quiescence and cooling. We use both fast and slow first rifting events, followed by a cooling period, producing diverse inherited initial conditions for the second rifting event. The common constrain for all models is an equal finite horizontal stretching for both rifting events, leading to longer (shorter) events in case of slow (fast) lithosphere extension. The cooling duration corresponds to the time needed for the lithosphere (thermal boundary layer) to recover the initial thickness.

The combination of fast and slow extension in two rifting events reveals that the same initial pristine lithosphere with identical initial conditions, can deform with many evolutionary strain patterns. These are unobserved in the models results, when a single rifting approach is used, unless the initial or the boundary conditions change for each model. This study shows that the multiple event rifting modelling approach leads to five different basin types and transition domains. Fast rifting events lead to narrow basins that were found to be less sensitive to rifting history, e.g. Red Sea, Rhine Graben, North Sea. All other basin types are strongly affected by prior rifting events, though to differing degrees. Repeated slow rifting events result in wide asymmetric basins, e.g. West Antarctic Rift Basin. As velocities during the second event become faster, wide basins generated by slow rifting in the first event become increasingly symmetric. The lithosphere progressively localizes along inherited heterogeneities. After an initial fast rifting extension, strong localized thinning of the crust occurs during a subsequent slow rifting event producing hyper-thinned crustal basins, e.g. Iberia Margin. The described basin type evolution highlights the role of heterogeneities developed during early history (e.g. inherited

structures) changes according to the boundary conditions used in the subsequent rifting event.

This study identifies cases when previous lithospheric rifting history cannot be neglected in modeling the evolution of sedimentary basins. Previous rifting, under a variety of conditions, consistently enhances localization in subsequent rifting events having a major effect on subsidence and melting histories of basins. When compared to models of single rifting events, the recovered subsidence rates for multiple rifting events are greatly affected in duration, pattern and magnitude. Modelling different rifting history can affect the interpretation of specific geologic cases, where anomalous subsidence and changes in subsidence rate, have been previously explained by a range of external processes or decreased internal lithospheric strength. Similarly, our study shows that melt volumes produced during rift basin formation, can be underestimated up to 30 times if modeled with a single rift event history when compared to models with complex multiple event histories.

Albeit simplified, our analysis provides an attempt to reduce the diverse complexities of natural basins into a general understanding, supporting future studies and interpretations of rifting evolution. Analyzing the entire model suite, it is possible to highlight rifting evolution patters otherwise unobserved. The study shows that the lithospheric strain modes can switch over time or co-exist at rifting cessation. Here, it is shown how the rift basin types selection, the transition between basin type domains and the amplification of inherited heterogeneities, are all affected by the variation of rifting history and boundary conditions.

Acknowledgment

We thank J.P. Brun, W.R. Buck, the Editors A. Revil and L. Wallace for comments to improve the manuscript, and G. Duclaux and S. Ellis for comments on an earlier version of this work. The Underworld code (http://www.underworldcode.org) is supported by AuScope Simulation, Analysis and Modelling (http://www.auscope.org.au/simulation-analysis-modelling/), Australian Research Council (http://www.arc.gov.au) and NeCTAR eResearch_tools (https://nectar.org.au). The data used are listed in the references and tables and are available upon request to the Authors.

APPENDICIES

A. Governing equations

We have modeled 2D lithospheric extension using Underworld geodynamics code (*Moresi et al.*, 2007; *Moresi et al.*, 2003). Underworld uses an Eulerian finite element mesh embedding Lagrangian material points to solve the Stokes flow problem and the energy (advection/diffusion) equation for large-scale deformation of visco-plastic materials.

The code solves the governing equations of mass (Eq.1A), momentum (Eq.2A), and energy conservation (Eq.3A) for an incompressible flow:

$$\frac{\partial u_i}{\partial x_i} = 0 \quad (1A)$$

$$\frac{\partial \tau_{ij}}{\partial x_j} - \frac{\partial p}{\partial x_i} = -\alpha \rho g T \qquad (2A)$$

$$\frac{\partial T}{\partial t} + u_i \frac{\partial T}{\partial x_i^2} = \kappa \frac{\partial^2 T}{\partial x_j^2} + H_r \qquad (3A)$$

where x_i are spatial coordinates, u_i velocity, $\boldsymbol{\tau_{ij}}$ deviatoric stress, p total pressure, α the coefficient of thermal expansion, ρ fluid density, T temperature, $\boldsymbol{g}$ gravity, κ the thermal diffusivity and H_r radiogenic heat.

The details of the numerical method, software implementation and relevant numerical benchmarks are described in *Moresi et al.* (2007) and *Moresi et al*. (2003). The code has been widely used in several geodynamic applications such as extension tectonics including passive margins (e.g. *Farrington et al.*, 2010; *Sharples et al*., 2015), subduction (e.g. *Stegman et al.*, 2010; *Capitanio and Replumaz*, 2013; *Capitanio*, 2014; *Mason et al*., 2010; *Farrington et al*., 2014) and for the study of the Stokes flow and problems arising in computational geodynamics (e.g. *May and Moresi*, 2008).

The constitutive equation relating stress to strain-rate is given by the generalized non-Newtonian model of the form:

$$\tau_{ij}^n = 2\eta \dot{\varepsilon}_{ij} \quad (4A)$$

where η is dynamic viscosity and $\dot{\varepsilon}$ the strain-rate tensor:

$$\dot{\varepsilon}_{ij} = \frac{1}{2}[\nabla u + (\nabla u)^T] \quad (5A)$$

We use a non-linear, temperature-dependent flow law for the viscous deformation of rocks with the following form:

$$\tau = \frac{1}{A \eta_{eff}^{n-1}} exp(\frac{E}{nRT}) \qquad (6A)$$

where R is the gas constant, A a pre-exponent, E the activation energy and n the power-law exponent (Table 1). The square root of the stress tensor's second invariant is defined as $\tau_{II} = \sqrt{\frac{\tau_{ij}\tau_{ij}}{2}}$.

The material parameters vary in the models according to the rock type (Table 1), that is we use rheological parameters of a wet quartzite for the upper crust (*Gleason*

and Tullis, 1995), wet diabase for the lower crust (*Mackwell et al.*, 1998) and a dry olivine for the mantle (*Chopra and Paterson*, 1981).

A Drucker-Prager frictional-plastic pressure-dependent law is used for brittle deformation (*Drucker and Prager*, 1952):

$$\tau_y = C_0 + tan(\varphi)\,\sigma_n \quad (7A)$$

where C_0 is the cohesive strength, $tan(\varphi)$ is the internal friction coefficient, φ is the internal friction angle, τ_y and σ_n are, respectively, the brittle shear and normal stress to the plane of failure within material (Table 1).

The composite visco-plastic flow law used in the models is implemented through an effective viscosity:

$$\eta_0 = min(\eta\,;\, \frac{\tau_y}{2\dot{\varepsilon}_{II}}) \quad (8A)$$

where $\dot{\varepsilon}_{II} = \sqrt{\frac{\dot{\varepsilon}_{ij}\dot{\varepsilon}_{ij}}{2}}$ is the square root of strain-rate tensor's second invariant, i.e. the effective strain rate.

B. Subsidence, Melting and Localization Index

The analysis of the models outputs are perfumed using, crust and mantle thinning factors, β and δ, (i.e. *Huismans et al.*, 2001; *England, 1983*; *van Wijk and Cloetingh*, 2002), melt production rates and volumes (i.e. *van Wijk et al.*, 2001) and lithosphere localization index (*Kaus and Podladchikov*, 2006; *Crameri and Kaus*, 2010; *Lu et al.*, 2011).

Crust and lithospheric mantle thinning factors

To ensure comparable outcomes, we measure the thinning factor for the crust and mantle, β and δ respectively. As we have defined the horizontal strain factor, $\varepsilon > 1$ for coherence with the plane homogeneous finite strain analysis, we should define $\beta$and δ as < 1. However, we have chosen to use the definition proposed by e.g. *van Wijk et al.* (2001), *van Wijk and Cloetingh* (2002), *England*, (1983), *Huismans et al.* (2001), with β and $\delta > 1$. This is because $\beta$is the ratio between the initial thickness of the crust, h_0, and the thickness at a later time, $h(x,t)$, hence h_0 is always > $h(x,t)$. Likewise, δ is calculated with the initial mantle thickness, H_0, which is always greater than the mantle thickness at the later time $H(x,t)$ (Table 1):

$$\beta(x,t) = h_o/h(x,t) \quad (1B)$$

$$\delta(x,t) = H_o/H(x,t) \qquad (2B)$$

We present the thinning factor for the whole crust and do not focus on details of intra-crustal structures. Following the definition of break-up of *Franke* (2013) we define the break-up of the crust when β> 22 and of the lithosphere when both β and δ > 22.

Subsidence

To reduce the impact of the modeling choice on the basin subsidence, we have calculated the tectonic subsidence in our models under the assumption of isostatic equilibrium following *Steckler and Watts* (1978) and *Watts* (2001) (Table 1).

$$S = \frac{a[(\rho_l - \rho_c)\frac{h}{a}(1-\frac{\alpha T_m h}{2a}) - \frac{\rho_l \alpha T_m}{a}](1-\frac{1}{\beta})}{\rho_l(1-\alpha T_m)-\rho_w} \qquad (3B)$$

where S is the tectonic subsidence (depth of the basement in absence of surface loads), ρ_l, ρ_c and ρ_w, are respectively the mantle lithospheric, crust and water averaged densities, T_m is the LAB temperature, α the coefficient thermal expansion and $\beta$the thinning factor of the whole crust. This choice allows the calculation of subsidence irrespective of the vertical absolute depth of the basin, which is advected as the lithospheric model stretches, and is calculated where the maximum thinning is measured. We assume that the crust top is at sea level prior to lithospheric extension and that it is progressively covered by water during subsidence (*McKenzie*, 1978). More importantly, Eq. 3B provides the directly tectonic contribution of the subsidence, the net of water and sediment loading.

Melt

Melting production is calculated using a benchmark model for peridotite formulated by *Katz et al.*, (2003) (Table 1). The *solidus* and *liquidus* curves for pressure are given by:

$$T_{sol} = A_1 + A_2 + A_3 p^2 \qquad (4B)$$
$$T_{liq} = B_1 + B_2 + B_3 p^2 \qquad (5B)$$

where A and B are fitting parameters (see *Katz et al.*, 2003). As T_{sol} and T_{liq} are computed in each element, we quantify the melt fraction D of peridotite at the temperature T as:

$$D = \left(\frac{T-(T_{Sol}-\Delta T_{H2O})}{T_{liq}-T_{Sol}}\right)^{\gamma 1} \quad (6B)$$

See *Katz et al.*, (2003) for an extensive explanation of parameterization used to calculate the melt fraction (A_n, B_n and γ_1 – originally β_1 in *Katz et al.*, 2003). The bulk water content, X_{H2O} of 0.02% integrated over the melt-generating area provides an estimate of melt and potential magma production. Latent heat is taken into account such as:

$$dT = \frac{LhD\rho_m}{C_p\rho_s} \quad (7B)$$

where dT is the change of temperature, Lh = 4.105 J kg^{-1}, is the latent heat D is the melt fraction, ρ_s is the solid density, ρ_m the density of the melt and C_p the heat capacity (*Turcotte and Schubert*, 2014) (Table 1). The latent heat of melting decreases the temperature, which in turn decreases the amount of partial melt. The melt assessment at each node follows an iterative scheme. We calculate melting as volume per unit width parallel to the rift axis, in the direction perpendicular to the 2D model.

Localization index

To highlight the feedback of the different lithospheric histories and strain modes (i.e. distributed vs localized strain) into the basin type and architecture, we follow *Kaus and Podladchikov* (2006), *Crameri and Kaus* (2010) and *Lu et al.* (2011), adopting a lithospheric strain localization index *I*. This approach has the advantage of containing both boundary and internal conditions, supporting inferences that are less model-constrained, and shows that for $I > 1$ conditions are met for strongly localized lithosphere strain, while for $I < 1$, it is distributed or weakly localized (Table 1).

The localization index accounts for the initial or background strain rates, the rheology and rate strain. *Crameri and Kaus* (2010) proposed a localization index *I* for lithospheric strain under compression:

$$I = \frac{\dot{\varepsilon}\,\Delta l}{1.4}\sqrt{\frac{\eta_0 E}{nRT^2 k}} \quad (8B)$$

where $\dot{\varepsilon}$ is the initial strain-rate, η_0 effective viscosity, E activation energy, n power law exponent, R gas constant, T temperature distribution, k the thermal conductivity and Δl a characteristic length. *Kaus and Podladchikov* (2006) proposed that the characteristic length Δl is the radius of a circular body enclosure, favoring stress localization. *Crameri and Kaus* (2010) instead used the thickness of the plastic field

(th_p). In their work the characteristic length in the 2D model was calculated using the gradient of the Moho morphology deflection, with localization occurring when steep gradients of $dy/dx > 4$ are found. *Lu et al.* (2011) used a similar approach, proposing as the characteristic length Δl, the Moho temperature anomaly deflection caused by lithospheric extension.

We find it useful here to adopt the same approach, illustrating the impact of rifting history as a deviation from the predicted localization. Additionally, we note that crustal thinning is similarly a measure of the height of the Moho's deflection with respect to original depth (*Crameri and Kaus*, 2010). Hence, we use the max Moho displacement as a characteristic length Δl for the localization index. In Eq. 8B, we replace Δl with $\Delta l = h_0 (1\text{-}1/\beta) - S$, using the initial crustal thickness h_0, the maximum thinning $\beta$and the subsidence S achieved in the first rifting event. This can be interpreted as an inherited condition, which implies the creation of distributed rifting-induced small perturbations when β is small (i.e. where the Moho presents crenulations distributed along the numerical domain, which serves as small distributed weak/strong seeds) or a single perturbation for large β, helping strain localization in early rifting events. As stated in Section 2.2, these perturbations can originate from the numerical approximation, intrinsic to the numerical model (*Peters et al.*, 2015). However, they are amplified here according to the velocity of boundary displacement.

REFERENCES

Anderson D.L. (1994). The sublithospheric mantle as the source of continental flood basalts; the case against the continental lithosphere and plume head reservoirs. *Earth and Planetary Science Letters*. 123(1-3):269-80.

Argus, D. F. and M. B. Heflin (1995). Plate motion and crustal deformation estimated with geodetic data from the Global Positioning System. *Geophysical Research Letters.* 22(15):1973-6.

Ali M.Y. and A.B. Watts (2013). Subsidence history, crustal structure, and evolution of the Somaliland - Yemen conjugate margin. *Journal of Geophysical Research:* Solid Earth. 118(4):1638-49.

Allen P.A. and J.R. Allen (2013). Basin analysis: Principles and application to petroleum play assessment. *John Wiley & Sons*. pp. 642

Allen P.A. and J.J. Armitage (2012), Cratonic basins, in *Syntectonic Basin Development, Active to Ancient: Recent Advances,* edited by C. Busby, *and* A. Azor, chap. 30:602–620, Wiley-Blackwell, Oxford.

Allen, P. A., P.G. Eriksson, F. F. Alkmim, P. G. Betts, O. Catuneanu, R. Mazumder, Q. Meng, and G. M. Young (2015). Classification of basins, with special reference to Proterozoic examples. *Geological Society, London, Memoirs.* 43(1):5-28.

Almalki K.A, P.G. Betts and L. Ailleres (2014). Episodic sea-floor spreading in the Southern Red Sea. Tectonophysics. 617:140-9.

Armitage J.J., J.S. Collier and T.A. Minshull (2010). The importance of rift history for volcanic margin formation. *Nature*. 465(7300):913-7.

Artyushkov, E. V. (2007). Formation of the superdeep South Caspian basin: subsidence driven by phase change in continental crust. *Russian Geology and Geophysics*. 48(12):1002-14.

Aslanian, D., M/ Moulin, J. Olivet, P. Unternehr, L. Matias, F. Bache, M. Rabineau H. Nouzé, F. Klingelheofer, I. Contrucci and C. Labails (2009). Brazilian and African passive margins of the Central Segment of the South Atlantic Ocean: Kinematic constraints. *Tectonophysics* 468(1): 98-112.

Aslanian D, M. Moulin (2010). Comment on 'A new scheme for the opening of the South Atlantic Ocean and the dissection of an Aptian salt basin'by Trond H. Torsvik, Sonia Rousse, Cinthia Labails and Mark A. Smethurst. *Geophysical Journal International*. 183(1):20-8.

Baker B.H, P.A, Mohr, L.A. Williams (1972). Geology of the eastern rift system of Africa. *Geological Society of America Special Papers*. 136:1-68.

Baldwin S., N. White and R.D. Müller (2006). Resolving multiple rift phases by strain-rate inversion in the Petrel Sub-basin, northwest Australia. *Geological Society of America Special Papers*. 372:245-63.

Bassi G. (1991):. Factors controlling the style of continental rifting: insights from numerical modelling. *Earth and Planetary Science Letters* 105(4) 430-452.

Bialas, R. W. and W.R. Buck (2009). The role of sedimentation in the development of rifts; Applications to the Gulf of California. *Tectonics*, 28, doi: 10.1029/2008TC002394

Birt, C. S., P. K. H. Maguire, M. A. Khan, H. Thybo, G.R. Keller and J. Patel (1997). The influence of pre-existing structures on the evolution of the southern Kenya Rift Valley - evidence from seismic and gravity studies. *Tectonophysics*. 278(1):211-42.

Bond G.C. and M.A. Kominz (1984). Construction of tectonic subsidence curves for the early Paleozoic miogeocline, southern Canadian Rocky Mountains: Implications for subsidence mechanisms, age of breakup, and crustal thinning. *Geological Society of America Bulletin*. 95(2):155-73.

Brun, J. P. (1999). Narrow rifts versus wide rifts: inferences for the mechanics of rifting from laboratory experiments, in *Philosophical Transactions of the Royal Society A*: Mathematical, Physical and Engineering Sciences, 357(1753).

Brune, S., A. A Popov and S. V. Sobolev (2012): Modeling suggests that oblique extension facilitates rifting and continental break-up. *Journal of Geophysical Research*, 117, B08402. doi:10.1029/2011JB008860.

Brune, S. and J. Autin (2013): The rift to break-up evolution of the Gulf of Aden: Insights from 3D numerical lithospheric-scale modelling. *Tectonophysics*, 607, 65-79. doi:10.1016/j.tecto.2013.06.029.

Brune, S., C. Heine, M. Perez-Gussinye and S.V. Sobolev (2014): Rift migration explains continental margin asymmetry and crustal hyper-extension. *Nature Communications*, 5, 4014. doi:10.1038/ncomms5014.

Brune, S., S. E., Williams, N. P Butterworth., and R. D. Müller. (2016). Abrupt plate accelerations shape rifted continental margins. *Nature* 536 (7615), 201-204.

Buck W.R. (1986). Small-scale convection induced by passive rifting: the cause for uplift of rift shoulders. *Earth and Planetary Science Letters*. 77(3):362-72.

Buck W.R. (1991) Modes of continental lithospheric extension. Journal of Geophysical Research, B, *Solid Earth and Planets* 96(12): 20161–20178.

Buck W.R., L.L. Lavier, and A.N.B. Poliakov (1999). How to make a rift wide. *Philosophical Transactions-Royal Society of London Series a Mathematical Physical and Engineering Sciences*. 671-89.

Buck W.R. (2004). Consequences of asthenospheric variability on continental rifting, in *Rheology and deformation of the lithosphere at continental margins*, *Columbia University Press, New York.,* 62:1–30.

Capitanio F.A., C. Faccenna and R. Funiciello (2009). The opening of Sirte basin: Result of slab avalanching?. Earth and Planetary Science Letters. 285(1):210-6.

Capitanio FA and A. Replumaz (2013). Subduction and slab breakoff controls on Asian indentation tectonics and Himalayan western syntaxis formation. *Geochemistry, Geophysics, Geosystems*. 14(9):3515-31.

Capitanio F.A. (2014). The dynamics of extrusion tectonics: Insights from numerical modeling. *Tectonics*. 33(12):2361-81.

Chen L. (2014). Stretching factor estimation for the long-duration and multi-stage continental extensional tectonics: Application to the Baiyun Sag in the northern margin of the South China Sea. *Tectonophysics*. 611:167-80.

Chenin P. and C. Beaumont (2013). Influence of offset weak zones on the development of rift basins: Activation and abandonment during continental extension and breakup. *Journal of Geophysical Research: Solid Earth*. 118(4):1698-720.

Chopra P.N, and M.S. Paterson (1984). The role of water in the deformation of dunite. *Journal of Geophysical Research*. 89: 7861–7876.

Corti G. (2012) Evolution and characteristics of continental rifting: Analog modeling-inspired view and comparison with examples from the East African Rift System. *Tectonophysics*. 522:1-33.

Corti G., I. Iandelli and M. Cerca (2013). Experimental modeling of rifting at craton margins. *Geosphere*, 9(1), 138–154, doi:10.1130/GES00863.1.

Crameri F. and B.J. Kaus (2010). Parameters that control lithospheric -scale thermal localization on terrestrial planets. *Geophysical Research Letters*. 37(9).

Crameri, F., H. Schmeling, G. J. Golabek, T. Duretz, R. Orendt, S. J. H. Buiter, D. A. May, B. J. P. Kaus, T. V. Gerya, and P. J. Tackley (2012). A comparison of numerical surface topography calculations in geodynamic modelling: an evaluation of the 'sticky air' method. *Geophysical Journal International*. 189(1):38-54.

Cunha T. (2008). Gravity anomalies, flexure and the thermo-mechanical evolution of the West Iberia margin and its conjugate of Newfoundland (*Doctoral dissertation, D. Phil thesis, University of Oxford.* 383pp).

Drucker D.C. and W. Prager (1952). Soil mechanics and plastic analysis or limit design. *Quarterly of applied mathematics*. 10.

England P. (1983). Constraints on extension of continental lithosphere. *Journal of Geophysical Research: Solid Earth*. 88(B2):1145-52.

Espurt, Nicolas, J.P.Callot, F. Roure, J.M. Totterdell, H.I.M. Struckmeyer and R. Vially (2012). Transition from symmetry to asymmetry during continental rifting: an example from the Bight Basin–Terre Adélie (Australian and Antarctic conjugate margins). *Terra Nova*. 24(3):167-80.

Farrington R.J., D.R. Stegman, L.N. Moresi, M. Sandiford, D.A. May (2010). Interactions of 3D mantle flow and continental lithosphere near passive margins. *Tectonophysics*. 483(1):20-8.

Farrington RJ, L.N. Moresi and F.A. Capitanio (2014). The role of viscoelasticity in subducting plates. *Geochemistry, Geophysics, Geosystems.* 4291-304.

Fernandez, M., and G. Ranalli (1997). The role of rheology in extensional basin formation modelling. *Tectonophysics*. 282(1):129-45.

Flament N., M. Gurnis, and R.D. Müller (2013). A review of observations and models of dynamic topography. *Lithosphere*. 5(2):189-210.

Flament, Nicolas, M. Gurnis, S. Williams, M. Seton, J. Skogseid, C. Heine, and R. D. Müller (2014). Topographic asymmetry of the South Atlantic from global models of mantle flow and lithospheric stretching. *Earth and Planetary Science Letters*. 387:107-19.

Franke D. (2013). Rifting, lithosphere breakup and volcanism: Comparison of magma-poor and volcanic rifted margins. *Marine and Petroleum Geology*. 43:63-87.

Gabrielsen R.H., T . Odinsen and I. Grunnaleite, (1999) Structuring of the Northern Viking Graben and the Møre Basin; the influence of basement structural grain, and the particular role of the Møre-Trøndelag Fault Complex. *Marine and Petroleum Geology*. 16(5):443-65.

Gleason G.C. and J. Tullis (1995). A flow law for dislocation creep of quartz aggregates determined with the molten salt cell. *Tectonophysics.* 247: 1–23.

Gueydan, F., C. Morency and J.-P. Brun (2008). Continental rifting as a function of lithosphere mantle strength. *Tectonophysics*, 460(1-4), 83–93. doi:10.1016/j.tecto.2008.08.012.

Heine C., R. D. Müller, B. Steinberger and T.H. Torsvik (2008). Subsidence in intracontinental basins due to dynamic topography. *Physics of the Earth and Planetary Interiors*. 171(1):252-64.

Heine, C., J., Zoethout and R.D. Mu□ller (2013). Kinematics of the South Atlantic rift. *Solid Earth*, 4(2), 215–253. doi:10.5194/se-4-215-2013

Huerta A.D. and D.L. Harry (2007). The transition from diffuse to focused extension: Modeled evolution of the West Antarctic Rift system. *Earth and Planetary Science Letters.* 255(1):133-47.

Hopper, J. R., T. Funck, B. E. Tucholke, H. C. Larsen, W. S. Holbrook, K. E. Louden, D. Shillington, and H. Lau. Continental breakup and the onset of ultraslow seafloor spreading off Flemish Cap on the Newfoundland rifted margin. *Geology* 32, no. 1 (2004): 93-96.

Huismans, R. S., and C. Beaumont (2007). Roles of lithospheric strain softening and heterogeneity in determining the geometry of rifts and continental margins. *Geological Society, London, Special Publication*s, 282(1), 111–138. doi:10.1144/SP282.6

Huismans, R., and C. Beaumont (2011). Depth-dependent extension, two-stage breakup and cratonic underplating at rifted margins. *Nature*, 473(7345), 74–8. doi:10.1038/nature09988

Huismans, R., and C Beaumont. (2014). Rifted continental margins: The case for depthdependent extension. *Earth and Planetary Science Letters* 407(2014)148–162.

Katz R.F., M. Spiegelman, and C. H. Langmuir (2003). A new parameterization of hydrous mantle melting. *Geochemistry, Geophysics, Geosystems*. 4(9).

Kaus, B.J., J.A.D Connolly, Y.Y. Podladchikov and S.M. Schmalholz (2005). Effect of mineral phase transitions on sedimentary basin subsidence and uplift. *Earth and Planetary Science Letters*. 233(1):213-28.

Kaus B.J. amd Y.Y. Podladchikov (2006) Initiation of localized shear zones in viscoelastoplastic rocks. *Journal of Geophysical Research: Solid Earth*. 111(B4).

Keen, C. E. (1985). The dynamics of rifting: deformation of the lithosphere by active and passive driving forces. *Geophysical Journal International*, 80(1), 95–120. doi:10.1111/j.1365-246X.1985.tb05080.x

Keen, C.E., (1987a) Dynamical extension of the Lithosphere during rifting: Some numerical model results, in *Composition, Structure and Dynamics of the Lithosphere-Asthenosphere System* pp. 189-203, edited by K.Fuchs and C. Froidveaux, Am. Geophys. Union, Geodynamics Series 16

Keen, C.E., (1987b) Some important consequences of lithospheric extension, in *Continental Extensional Tectonics* edited by M.P. Coward, J.F. Dewey, and P.L. Hancock, pp. 67-73, Geological Society Special Publication no. 28

Keen C.E. and R.R. Boutilier (1995). Lithosphere-asthenosphere interactions below rifts. In *Rifted Ocean-continent boundaries*, pp. 17-30, Springer Netherlands.

Keen C.E. And R.R. Boutilier (2000). Interaction of rifting and hot horizontal plume sheets at volcanic margins. *Journal of Geophysical Research: Solid Earth*. 105(B6):13375-87.

Koopmann H., S. Brune, D. Franke and S. Breuer (2014). Linking rift propagation barriers to excess magmatism at volcanic rifted margins. *Geology*. 42(12):1071-4.

Kusznir, N.J., and R. G. Park (1987). The extensional strength of continental lithosphere: Its dependence on geothermal gradient, and crustal composition and thickness, in *Continental Extensional Tectonics*, edited by M.P. Coward, J. F. Dewey, and P.L. Hancock, *Spec. Publ. Geol. Soc. London*, 28, 35-52, 198. doi:10.1144/GSL.SP.1987.028.01.04.

Lavier, L. L., and G. Manatschal, (2006). A mechanism to thin the continental lithosphere at magma-poor margins. *Nature*, 440(7082), 324–8. doi:10.1038/nature04608

Lu G., B.J. Kaus and L. Zhao (2011). Thermal localization as a potential mechanism to rift cratons. *Physics of the Earth and Planetary Interiors*. 186(3):125-37.

Lyngsie S.B., H. Thybo and R. Lang (2007). Rifting and lower crustal reflectivity: A case study of the intracratonic Dniepr-Donets rift zone, Ukraine. *Journal of Geophysical Research: Solid Earth*. 112(B12).

Mackwell S.J., M.E. Zimmerman and D.L. Kohlstedt (1998) Hightemperature deformation of dry diabase with applications to tectonics on Venus. *Journal of Geophysical Research*, 103: 975–984.

Manatschal G, L. Lavier and P. Chenin. (2015) The role of inheritance in structuring hyperextended rift systems: Some considerations based on observations and numerical modeling. *Gondwana Research*., 27(1):140-64.

Marotta A. M., U. Bayer and H. Thybo (2000). The legacy of the NE German Basin - reactivation by compressional buckling. *Terra Nova.* 12(3):132-40.

Mason W.G., L. Moresi, P.G. Betts and M.S. Miller (2010). Three-dimensional numerical models of the influence of a buoyant oceanic plateau on subduction zones. *Tectonophysics.* 483(1):71-9.

May D.A. And L. Moresi (2008). Preconditioned iterative methods for Stokes flow problems arising in computational geodynamics. *Physics of the Earth and Planetary Interiors.* 171(1):33-47.

McClusky S, R. Reilinger, G. Ogubazghi, A. Amleson, B. Healeb, P. Vernant, J. Sholan, S. Fisseha, L. Asfaw, R. Bendick and L. Kogan (2010). Kinematics of the southern Red Sea–Afar Triple Junction and implications for plate dynamics. *Geophysical Research Letters*. 37(5).

McKenzie, D. (1978), Some remarks on the development of sedimentary basins, *Earth Planet. Sci. Lett*., 40(1), 25–32.

Moresi L, F. Dufour and H.B. Mühlhaus (2003). A Lagrangian integration point finite element method for large deformation modeling of viscoelastic geomaterials. *Journal of Computational Physics*.184(2):476-97.

Moresi L, S. Quenette, V. Lemiale, C. Meriaux, B. Appelbe and H.B. Mühlhaus (2007). Computational approaches to studying non-linear dynamics of the crust and mantle. *Physics of the Earth and Planetary Interiors*. 163(1):69-82.

Moulin, M., D. Aslania., and E. Al (2005). Geological constraints on the evolution of the Angolan margin based on reflection and refraction seismic data (ZaïAngo project). *Geophysical Journal International*. 162(3):793-810.

Naliboff J. and S.J. Buiter (2015). Rift reactivation and migration during multiphase extension. *Earth and Planetary Science Letters*. 421:58-67.

Newman, R. and N. White (1997). Rheology of the continental lithosphere inferred from sedimentary basins. *Letter of Nature*, 385(13):621–624.

Perez-Gussinye, M. (2012). A tectonic model for hyperextension at magma-poor rifted margins : an example from the West Iberia − Newfoundland conjugate margins service Subscribe A tectonic model for hyperextension at magma-poor rift. *Geological Society, London, Special Publications*, 369(1), 403–427. doi:10.1144/SP369.19.

Pérez-Gussinyé M., J. Morgan, T. Reston and C. Ranero, (2006). The rift to drift transition at non-volcanic margins: Insights from numerical modelling. *Earth and Planetary Science Letters*, 244(1-2), 458–473. doi:10.1016/j.epsl.2006.01.059.

Péron -Pinvidic G. and G. Manatschal (2010) -- From microcontinents to extensional allochthons : witnesses of how continents break apart?. Petroleum Geosciences. Vol. 16, pp. 189–197, doi: 10.1144/1354-079309-903.

Péron-Pinvidic, G., G. Manatschal, E. Masini, E. Sutra, J. M. Flament, I. Haupert, and P. Unternehr (2015). Unravelling the along-strike variability of the Angola–Gabon rifted margin: a mapping approach, in *Petroleum Geoscience of the West Africa Margin*., vol. 438, edited by Sabato C., T., Hodgkinson, R. A. & Backe, G. , pp GSL London, Special Publications, http://doi.org/10.1144/SP438.1http://doi.org/10.1144/SP438.1

Peters M., M. Veveakis, T. Poulet, A. Karrech, M. Herwegh, and K. Regenauer-Lieb (2015). Boudinage as a material instability of elasto-visco-plastic rocks. *Journal of Structural Geology*. 78:86-102.

Petersen K.D., J.J. Armitage, S.B. Nielsen and H. Thybo (2015). Mantle temperature as a control on the time scale of thermal evolution of extensional basins. *Earth and Planetary Science Letters*. 409:61-70.

Petrini, K. A. T. E., J. A. D. Connolly,and Y. Podladchikov (2001). A coupled petrological–tectonic model for sedimentary basin evolution: the influence of metamorphic reactions on basin subsidence. *Terra Nova*. 13(5):354-9.

Reemst P. and S. Cloetingh (2000). Polyphase rift evolution of the Vøring margin (mid Norway): constraints from forward tecto
Tectonics. 19(2):225-40.

Reilinger R. and S. McClusky (2011). Nubia–Arabia–Eurasia plate motions and the dynamics of Mediterranean and Middle East tectonics. *Geophysical Journal International*. 186(3):971-9.

Sharples W, L.N. Moresi, M.A. Jadamec, and J. Revote (2015). Styles of rifting and fault spacing in numerical models of crustal extension. *Journal of Geophysical Research: Solid Earth*.120(6):4379-404.

Schmeling H. (2010). Dynamic models of continental rifting with melt generation. *Tectonophysics*. 480(1):33-47.

Şengör A.C. and B.A. Natal'in (2001). Rifts of the world. *Geological Society of America Special Papers*. 352:389-482.

Steckler, M. S., and A. B. Watts (1978). Subsidence of the Atlantic-type continental margin off New York. *Earth and Planetary Science Letters.* 41(1):1-3.

Stegman D.R., R. Farrington, F.A. Capitanio and W.P. Schellart (2010). A regime diagram for subduction styles from 3-D numerical models of free subduction. *Tectonophysics*. 483(1):29-45.

Sutra, Emilie, and G. Manatschal (2012). How does the continental crust thin in a hyperextended rifted margin? Insights from the Iberia margin. *Geology*. 40(2):139-42.

Sutra E., G. Manatschal, G. Mohn and P. Unternehr (2013). Quantification and restoration of extensional deformation along the Western Iberia and Newfoundland rifted margins. *Geochemistry, Geophysics, Geosystems.* 14(8):2575-97.

Tett, D.L., and D.S. Sawyer (1996).Dynamic models of multiphase continental rifting and their implications for the Newfoundland and Iberia Conjugate margins. In *Proceedings-Ocean Drilling Program Scientific Results* (Pp. 635-648). National Science Foundation.

Turcotte DL, Schubert G. (2014). Geodynamics. *Cambridge University Press*, pp. 636.

Unternehr, P., G. Peron-Pinvidic, G. Manatschal and E. Sutra (2010). Hyper-extended crust in the South Atlantic: in search of a model. *Petroleum Geoscience*, 16(3), 207–215. doi:10.1144/1354-079309-904

van Wees J.D., A. Arche, C.G. Beijdorff, J. López-Gómez and S.A. Cloetingh (1998). Temporal and spatial variations in tectonic subsidence in the Iberian Basin (eastern Spain): inferences from automated forward modelling of high-resolution stratigraphy (Permian–Mesozoic). *Tectonophysics*. 300(1):285-310.

van Wijk, J. W., R. S. Huismans, M. Ter Voorde, and S. A. P. L. Cloetingh (2001). Melt generation at volcanic continental margins: no need for a mantle plume. *Geophysical Research Letters*. 28(20):3995-8.

van Wijk J.W. and S.A. Cloetingh (2002). Basin migration caused by slow lithospheric extension. *Earth and Planetary Science Letters*. 198(3):275-88.

Watts A.B. (2001). Isostasy and Flexure of the Lithosphere. *Cambridge University* Press, pp. 480.

Weinberg RF, K, Regenauer-Lieb and G. Rosenbaum (2007). Mantle detachment faults and the breakup of cold continental lithosphere. *Geology*, 35(11):1035-8.

Wernicke, B. (1985) Uniform-sense simple shear of the continental lithosphere. *Can. J.Earth. Sci.* 22, 108–25.White, R. S. and D. P. McKenzie. (1989). Volcanism at rifts. *Sci. American*, July: 62-71. 9.

Whitmarsh, R. B., G. Manatschal, and T. A. Minshull (2001). Evolution of magma-poor continental margins from rifting to seafloor spreading. *Nature* 413(6852): 150-154.

Zelt, C. A., K. Sain, J. V. Naumenko, and D. S. Sawyer (2003). Assessment of crustal velocity models using seismic refraction and reflection tomography. *Geophysical Journal International*, 153: 609 – 626.

Table 1. Thermal and mechanical parameters of the lithosphere used in model simulations

Parameter	Abbreviation	Unit	Range/Value	Notes	References
Initial total crust thickness	h	km	30		
Initial upper crust thickness	h_{UC}	km	15		
Initial lower crust thickness	h_{LC}	km	15		
Lithosphere thickness	a	km	100		
Model initial width	L_o	km	400 464	Onset Rift 1 Onset Rift 2	
Total horizontal strain	ε	Dimensionless	1.32		
Crust thinning factor	β	Dimensionless			
Lithospheric mantle thinning factor	δ	Dimensionless			
Horizontal extension velocity	v	cm/yr			1, 2, 3
			0.05, 0.1, 0.15, 0.2, 0.25, 0.3, 0.35, 0.4, 0.45, 0.5, 0.75, 1, 1.25, 1.5, 2, 2.5, 3	v<0.45 cm/yr is referred to as Slow v>0.5 cm/yr is referred to as Fast	
Horizontal extension velocity, end-members models	v_{slow}	cm/yr	0.15		
	v_{fast}	cm/yr	2.5		
Initial strain rate	$\dot{\varepsilon}_{1,2} = 2\,v / L_o$	s^{-1}	7.9×10^{-17} s^{-1} to 4.7×10^{-15} s^{-1}	$\dot{\varepsilon}_{in1}$ Rift 1	
			6.8×10^{-17} to 4.1×10^{-15}	$\dot{\varepsilon}_{in2}$ Rift 2	
Péclet number	Pe	Dimensionless			

Models symbols and event duration			
Slow rifting event	r		
Fast rifting event	R		
Cooling periods	C_q, c_q		
Rifting duration	t_r	Myr	
Cooling duration	t_c	Myr	
Thermal parameters and variables			
Thermal conductivity	k	$Wm^{-1}\ K^{-1}$	2.6
Thermal diffusivity	κ	$m^2\ s^{-1}$	10^{-6}
Crust radioactive production	H_r	$W\ m^{-3}$	$1.2x10^{-6}$
Temperature	T	^oC	
Temperature profile - crust	T_c	^oC	
Temperature profile – lithospheric mantle	T_m	^oC	
Surface temperature	T_0	^oC	0
Lithosphere-Asthenosphere Boundary (LAB)	T_{lab}	^oC	1300
Heat flux from the mantle	Q_m	mW/m^2	30^{-3}
Thermal expansion	α	$10^{-5}\ C^{-1}$	3
Mechanical parameters and variables			
Upper Crust density	ρ_{uc}	$kg\ m^{-3}$	2700
Lower Crust density	ρ_{lc}	$kg\ m^{-3}$	2900
Crust density average	ρ_c	$kg\ m^{-3}$	2800
Lithospheric mantle density	ρ_l	$kg\ m^{-3}$	3300
Cohesion	C_o	MPa	60
Friction coefficient	$tan(\varphi)$	Dimensionless	0.6
Strain rate and second invariant	$\dot{\varepsilon}_{ij}$, $\dot{\varepsilon}_{II}$	s^{-1}	
Gravity Constant	g	$m\ s^{-2}$	9.81
Deviatoric stress, stress second invariant and brittle yielding stress	τ_{ij}, τ_{II}, τ_y	MPa	
Lithostatic Pressure	p	MPa	
Power law parameters			
Universal Gas Constant	R	$J(mol\ K)^{-1}$	8.314
Viscosity, Effective viscosity	η, η_0	Pa s	

Activation energy	E	J mol^{-1}	223	UC	4
			485	LC	5
			535	LM	6
Stress exponent	n	Dimensionless	4	UC	4
			4.7	LC	5
			3.6	LM	6
Pre-exponent constant	A	MPa^{-n} s^{-1}	$1.1x10^{-4}$	UC	4
			190	LC	5
			4.5	LM	6
Localization index calculation					
Moho's height deflection 2D models	Δl	km			
Localization index	I	Dimensionless			
Subsidence calculation					7
Tectonic Subsidence	S	M Myr^{-1}			
Water density	ρ_w	Kg m^{-3}	1000	*Initial* ρ_c, ρ_l, α, T_m, a, h as for previous	
Melting calculation					8
Solidus Temperature	T_{sol}	^oC			
Liquidus Temperature	T_{liq}	^oC			
Melt fraction	D	%			
Fitting parameters	A_1, A_2, A_3	^oC, ^oC GPa^{-1}, ^oC GPa^{-2}	1085.7, 132.9, -5.1	To calculate T_{sol}	8
	B_1, B_2, B_3	^oC, ^oC GPa^{-1}, ^oC GPa^{-2}	1475.0, 80.0, -3.2	To calculate. T_{liq}^{lherz}	8
	C_1, C_2, C_3	^oC, ^oC GPa^{-1}, ^oC GPa^{-2}	1780.0, 45.0, -2.0	To calculate T_{liq}	8
Exponents of the melting function	γ_1	Dimensionless	1.5	To calculate D (β_1 in Katz et al., 2003)	8
Bulk distribution coefficient of water between solid peridotite and melt	D_{H2O}		0.01		8
Latent heat	Lh	J kg^{-1}	4.105		9
Heat capacity	Cp	J kg^{-1} $^oC^{-1}$	1000		9
Solid density (mantle)	ρ_s	kg m^{-3}	3300		9
Melt density	ρ_m	kg m^{-3}	2900		9

1- *Argus and Hefin* (1995); 2 - *Reilinger R., and McClusky*, 2011; 3 - *McClusky et al.* (2010); 4, *Gleason and Tullis* (1995): 5 - *Mackwell et al.* (1998); 6 - *Chopra and Paterson* (1981); 7 - *Watts* (2001); 8 - *Katz et al.* (2003); 9 - *Turcotte and Schubert* (2002)

FIGURE CAPTIONS

Figure 1. Numerical model setup. The lithosphere is 100 km thick and defined by the 1300 °C isotherm, with the upper and lower crust 15 km thick each, and sticky air-like layer on top. Beneath the lithosphere, the asthenosphere extends to the bottom of the computational domain, at 700 km depth. Divergent horizontal velocity boundary conditions of $\pm v$ are applied at the right and left sides of the numerical domain (v range is 0.05-3 cm/yr). The velocity boundary conditions on the top and bottom wall are free-slip. The temperature profile is depth-dependent and constant laterally. No initial perturbations are added. The stress profile is calculated according to Eq. 6A, 7A and 8A with $\dot{\varepsilon}=1x10^{-15}$ s^{-1}.

Figure 2. Plot of crustal and lithospheric mantle thinning factors β and δ by domain width vs. time, showing the switch between distributed and localize strain modes in time for the crust and mantle. Velocity boundary conditions for slow (r_1 and r_2) and fast (R_1 and R_2) rifting events are v_{slow} = 0.15 cm/yr and v_{fast} = 2.5 cm/yr, respectively. (a) Models with repeated slow rifting r_1-r_2, (b) slow and fast rifting events r_1-R_2, (c) fast and slow rifting events R_1-r_2, and (d) repeated fast rifting events R_1-R_2.

Figure 3. Thinning factors (top) and strain rate second invariant (bottom) for models r_1-r_2, r_1-R_2 R_1-r_2 and R_1-R_2.. Velocity boundary conditions as per Fig. 2. Top panels show thinning factors for crust, β(black solid line), and lithospheric mantle, δ (black dashed line). Bottom panels show the second invariant of the strain-rate, $\dot{\varepsilon}_{II}$, with upper crust, lower crust and Moho (green lines), initial (black line) and thermally perturbed (red line) LAB. (a) r_1, at the end of the first slow rifting event. (b) r_1-r_2, at the end of the second slow rifting event. (c) r_1-R_2, at the end of the model with slow early rifting event followed by fast second rifting event. (d) R_1: at the end of the first fast rifting event showing a localized lithospheric strain mode (e) R_1-r_2, model with repeated fast rifting, with hyper-thinned crust above a mildly thinned mantle. (f) R_1-R_2, shows the end of the model with fast early rifting and second rifting.

Figure 4. Subsidence curves for multiple rifting event models (r_1-r_2 in blue, r_1-R_2 in orange, R_1-r_2 in red, R_1-R_2 in green) and single rifting event models (M_0, M_1 and M_2, black lines). Breakup is indicated to better characterize the full rifting history: the white star indicate crust break-up (C) and black star the indicate the whole lithospheric break-up (crust C and lithospheric mantle LM). Velocity boundary conditions: for multiple rifting event models as per Fig. 2; Constant boundary velocity for single event rifting models for single rifting event models, M_0, v = 0.05 cm/yr; M_1 v_{slow} = 0.15 cm/yr; M_2, v_{fast} = 2.5 cm/yr. Numbers indicated changes in boundary velocity. Subsidence rates for the end-member multiple rifting events are detailed in the results section. M_0 (segment 1-10) reaches 900 m of subsidence in 70 Myr without breakup. Model r_1-r_1, R_1-r_2 and M_1 share the 1-2 segment: the subsidence at point 2 is 800 m. From point 2, M_1 (segment 2-11) reaches ~1100 m of subsidence in the first 30 Myr, and a maximum subsidence of ~ 1250 m in the following 20 Myr stopping at point 11 (~53 Myr). Segment 2-3 is the thermal subsidence for r_1-r_1 and R_1-r_2. From point 3, model r_1-r_1 subsidence proceeds until 42 Myr with a similar rate of segment 1-2, then increases until 48 My, to then deflect upwards and stop at point 4 where the max subsidence ~2100 m (56Myr). From point 3 model r_1-R_1 continues until point 5 at 31Myr, with a max subsidence of ~ 1150 m. Model R_1-r_1, R_1-R_2 and M_2 share the segment 1-6: the subsidence at point 6 is 1100 m (~ 3 Myr). From point 6, M_2 (segment 1-12) reaches ~ 1950 m of subsidence in less of 3 Myr, before

breakup at point 12 (black star). From point 6, M_2 reaches ~ 1950 m of subsidence in less of 3 Myr, before breakup at point 12 (black star). Segment 6 -7 is the thermal subsidence for R_1-r_1 R_1-R2: the thermal subsidence reaches a total depth of ~ 1700 m at 25 Myr. From point 7, model R_1-r_1 proceeds until 31 Myr, with a similar rate of previous thermal subsidence in segment 5-7, to then dramatically increases until point 8, where the max subsidence is 2650 m (~36 Myr). From point 7, model R_1-R_1 proceeds until point 9 where it reaches a max subsidence of ~ 2000 m (27 Myr), reaching full breakup (black star). The comparison between single and multiple event rifting models highlights the role of deformation (rifting) history on subsidence patters and basin depocenter depth.

Figure 5. Melt production. (a) Melt volume rates (km^3/Myr) and (b) Integrated melt volume (km^3) with model r_1-r_2 (blue curve), r_1-R_2 (orange), R_1-r_2 (red) and R_1-R_2.(green). The melt volume is calculated as model domain (area in km^2) per unit width (1 km) parallel to the rift axis, in the direction perpendicular to the 2D model. (c) Post-processing melt percentage contours plotted on second invariant of strain-rate, and upper crust (top), lower crust (middle) and Moho (bottom) black lines at the end of the rift event. (1) and (2) r_1,-r_2; (3) and (4) r_1,-R_2; (5) and (6) R_1,-r_2; (7) and (8) R_1-R_2 Parameters: after Katz et al., (2003). Comparing the 4 end-member models for multiple event rifting events, highlights the role of rifting history on the melt production and distribution at depth.

Figure 6. (a) Basin type domain diagram for 289 numerical models of two rifting events separated by cooling, in $\dot{\varepsilon}_1$ vs $\dot{\varepsilon}_2$ space, being the initial strain-rates at the onset of the first and second rifting events, respectively. The following domains are divided in two groups: “slow first rifting-controls” group with Sag-like Basin (SB), Asymmetric Wide Basin (AWB), and Symmetric Wide Basin (SWB); “fast first rifting-controls” group with Narrow Basin (NB) and Hyper-Thinned Crustal Basin (HTB). In grey, the rift style is transitional and has mixed features. Larger dots are the reference end-member models r_1-r_2, r_1-r_2, R_1-r_2 and R_1-R_2 (Fig. 2. 3, 4 and 5). (b) Localization indexes domain diagram for the 289 numerical models indicating lithospheric strain modes, in a $\dot{\varepsilon}_1$ vs $\dot{\varepsilon}_2$ space. The color map shows the calculated localization index I_2 in the second event for each model with SB, AWB, SWB, NB, HTB basin types domains. The vertical black dashed line is the projection of the thresholds value localization index I_1 =1 between distributed (I_1 < 1, “slow first rifting-controls” group) and localized (I_1 >1 “fast first rifting-controls” group) lithospheric strain for the first rifting event of an extending pristine lithosphere (see text). The figures (a) and (b) represent models data domains, allowing recognition of rifting patterns otherwise unobserved: the comparison between analytical and

modeled localization indexes illustrates the domains where previous lithospheric strain history controls tectonic evolution of the basin types.

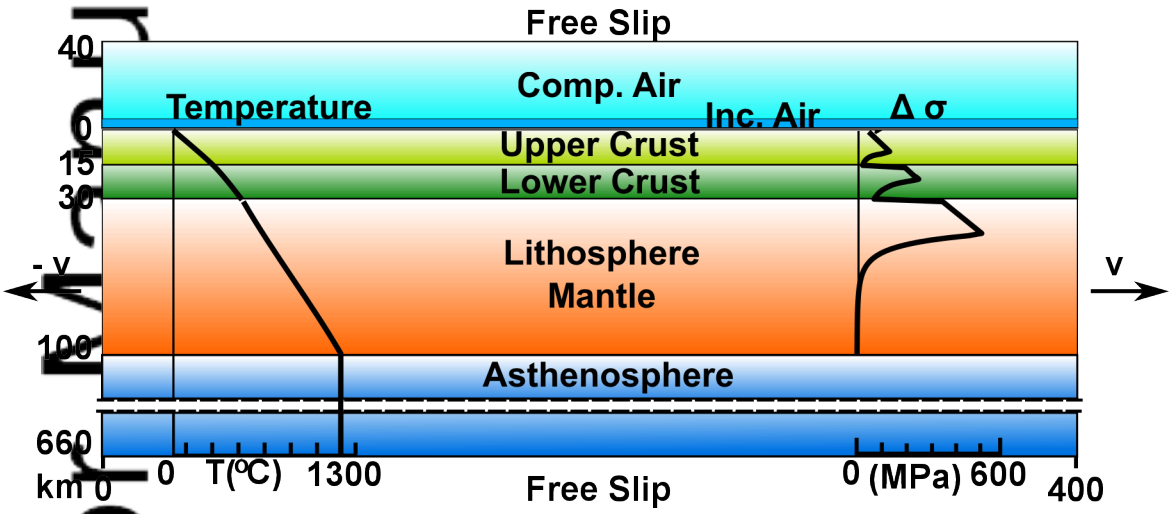

2016jb013005-f01-z-.eps

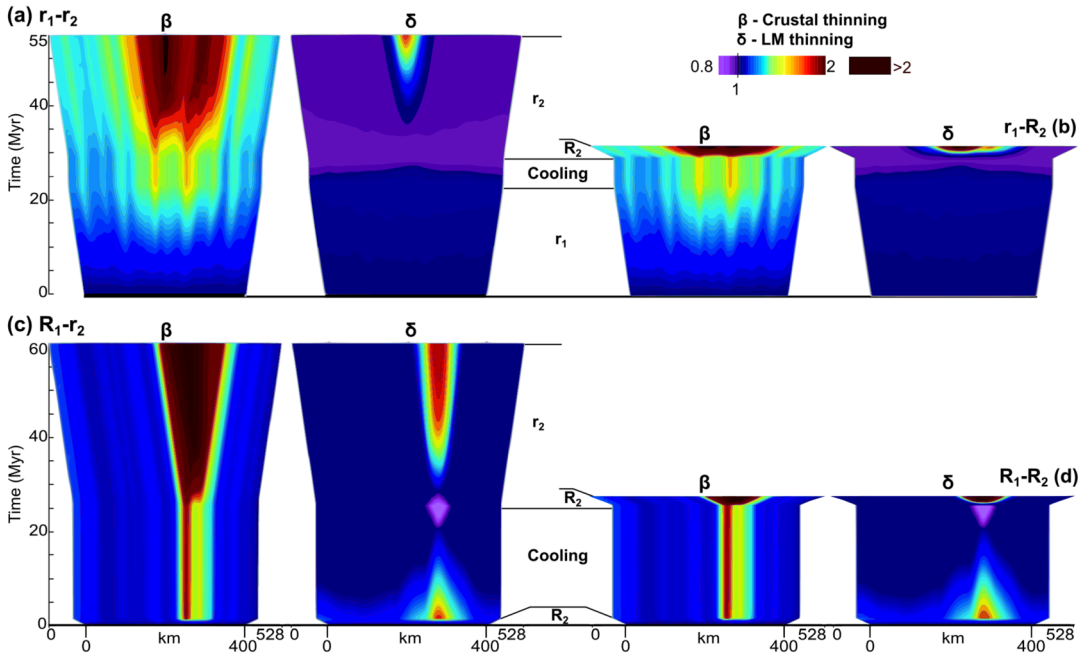

2016jb013005-f02-z-.eps

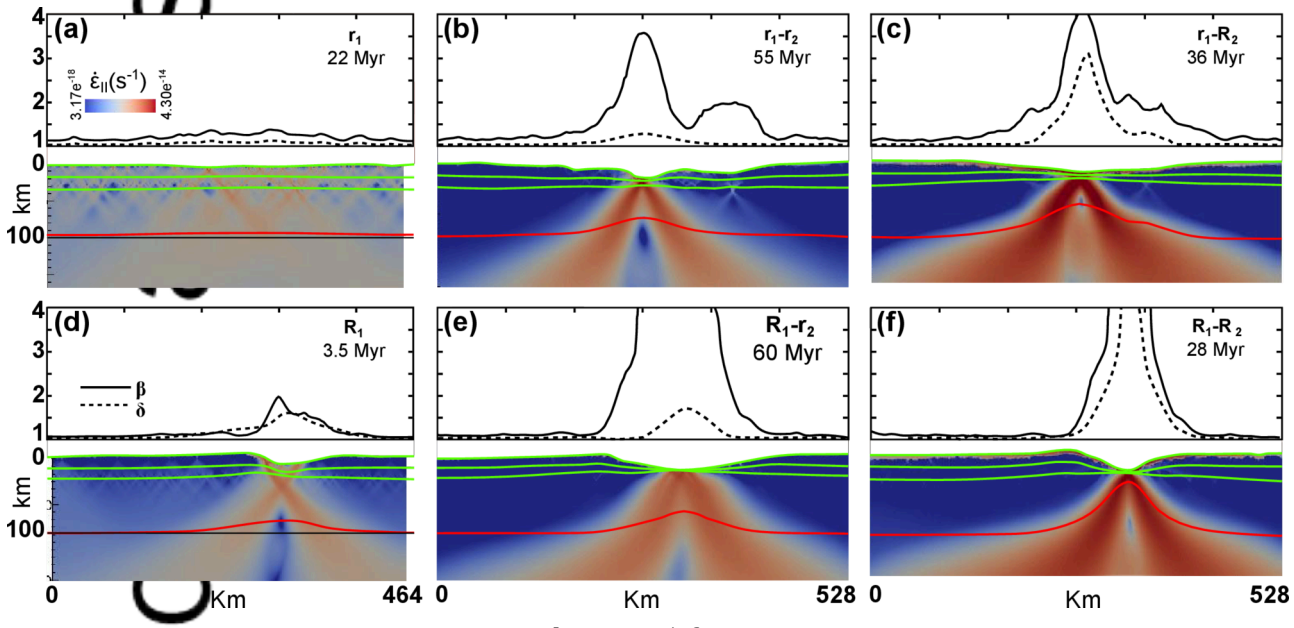

2016jb013005-f03-z-.eps

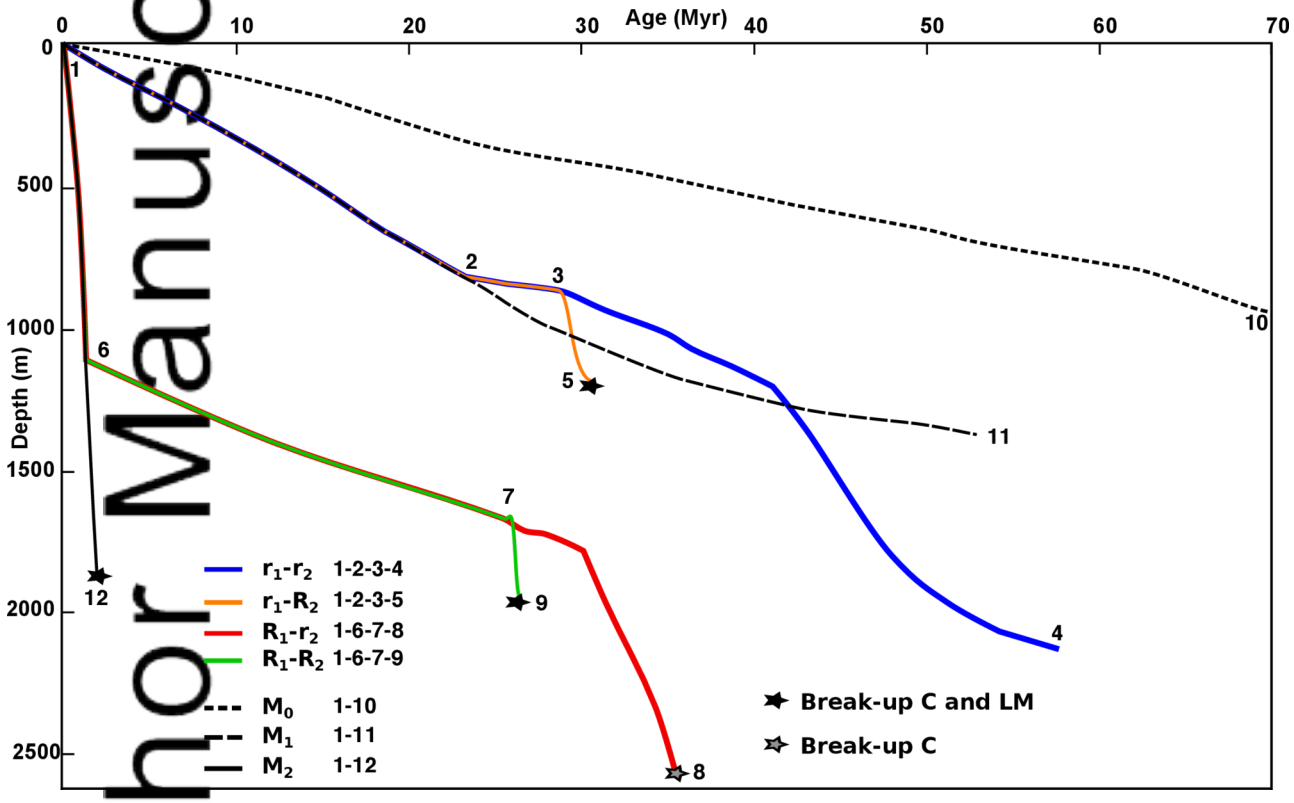

2016jb013005-f04-z-.eps

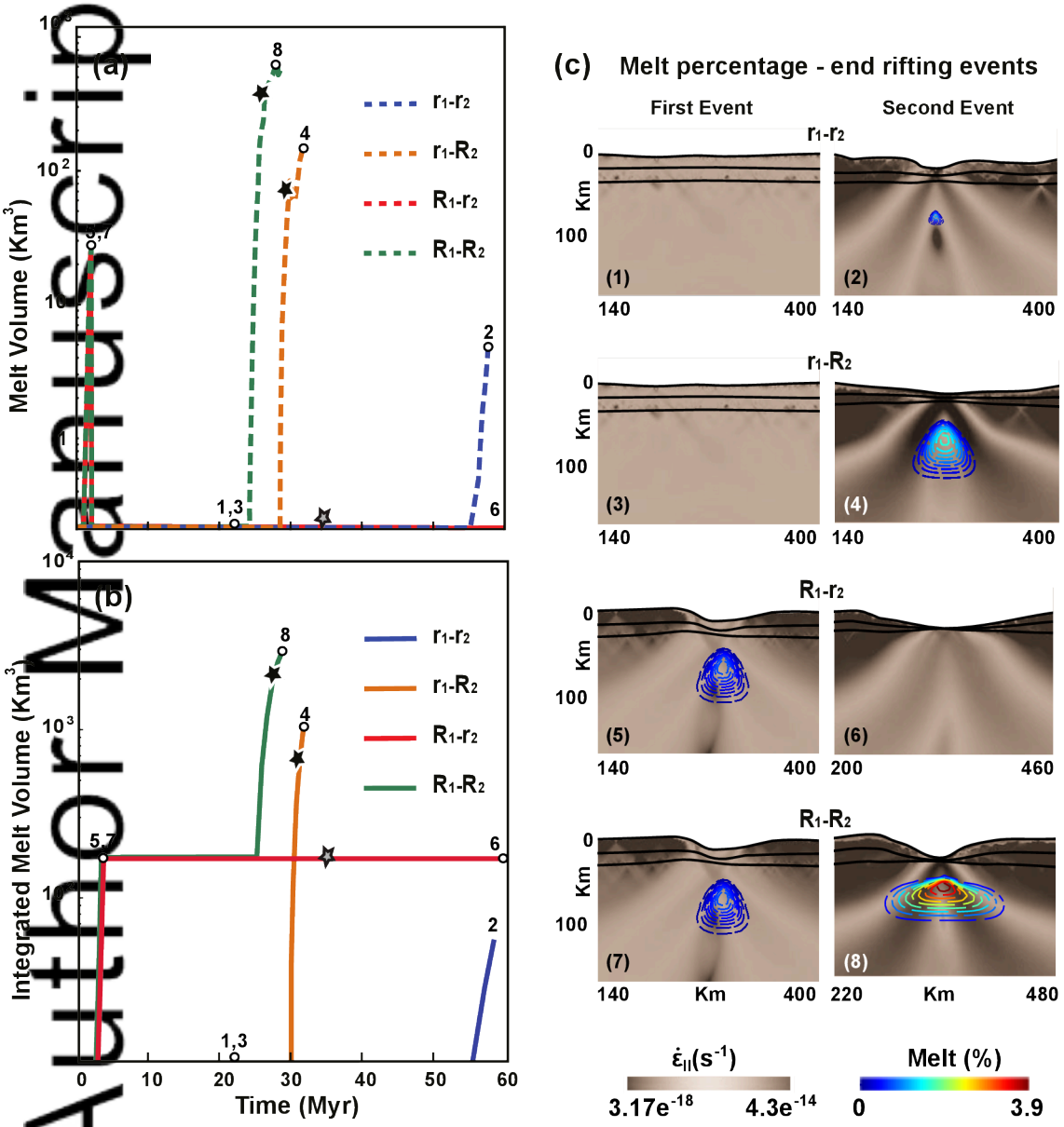

2016jb013005-f05-z-.eps

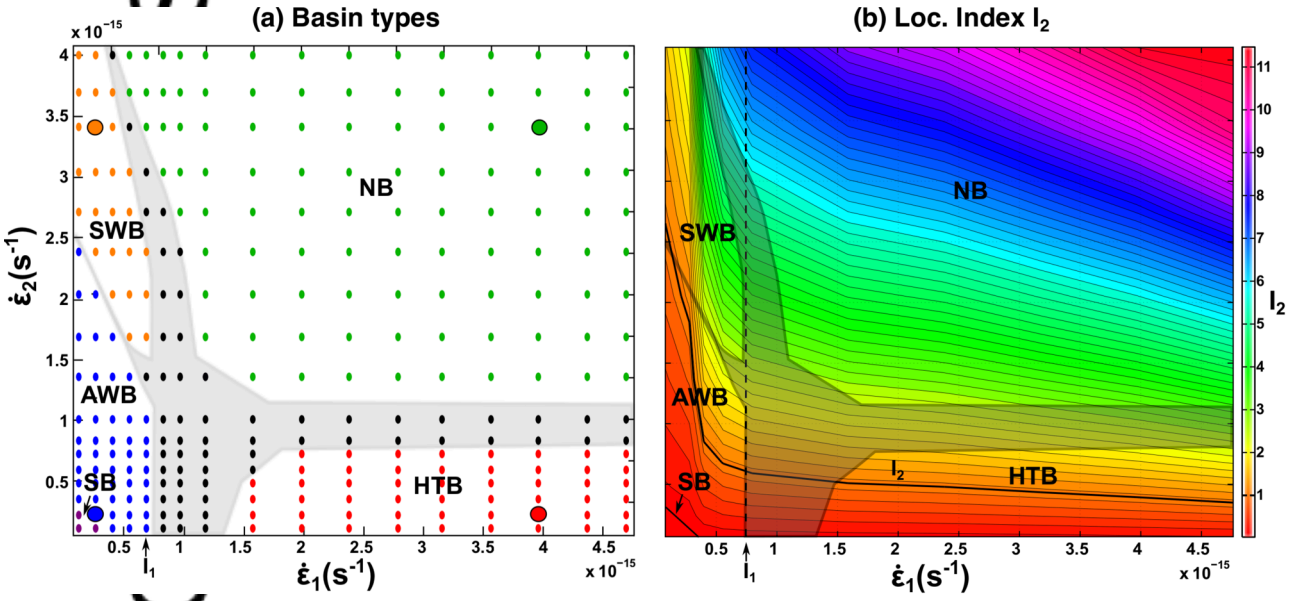

2016jb013005-f06-z-.eps